

An Accurate Flux Density Scale from 1 to 50 GHz

R. A. Perley and B. J. Butler

RPerley@nrao.edu, BButler@nrao.edu

National Radio Astronomy Observatory

P.O.Box O, Socorro, NM, 87801

Received _____; accepted _____

Intended for the Astrophysical Journal, Supplement Series

ABSTRACT

We develop an absolute flux density scale for cm-wavelength astronomy by combining accurate flux density ratios determined by the VLA between the planet Mars and a set of potential calibrators with the Rudy thermophysical emission model of Mars, adjusted to the absolute scale established by WMAP. The radio sources 3C123, 3C196, 3C286 and 3C295 are found to be varying at a level of less than $\sim 5\%$ per century at all frequencies between 1 and 50 GHz, and hence are suitable as flux density standards. We present polynomial expressions for their spectral flux densities, valid from 1 to 50 GHz, with absolute accuracy estimated at 1 – 3 % depending on frequency. Of the four sources, 3C286 is the most compact and has the flattest spectral index, making it the most suitable object on which to establish the spectral flux density scale. The sources 3C48, 3C138, 3C147, NGC7027, NGC6542, and MWC349 show significant variability on various timescales. Polynomial coefficients for the spectral flux density are developed for 3C48, 3C138, and 3C147 for each of the seventeen observation dates, spanning 1983 through 2012. The planets Venus, Uranus, and Neptune are included in our observations, and we derive their brightness temperatures over the same frequency range.

Subject headings: Instrumentation:interferometers, Methods: data analysis, observational, Techniques: interferometric, Telescopes(VLA)

1. Introduction

The flux density scale most commonly used at centimeter wavelengths is based on the spectral flux densities listed in Baars *et al.* (1977) for the four strong radio sources Cassiopeia A, Cygnus A, Taurus A, and Virgo A. The data utilized in that paper were taken by many radio telescopes, mostly in total power. The measured spectral flux densities of these four sources were termed by Baars *et al.* (1977) as ‘absolute’, meaning the telescopes utilized had accurately known gains and the observations were calibrated with a suitable thermodynamic standard. The Baars *et al.* (1977) paper provides convenient polynomial expressions for the spectral flux densities for these four sources, valid between 30 MHz and 30 GHz, with an accuracy estimated at about 5%. However, because all four of these primary flux density sources have angular sizes of several arcminutes, none is suitable as a calibrator for modern high resolution interferometers.

To provide a more widely distributed network of potential calibrators, Baars *et al.* (1977) also included polynomial expressions – generally valid from 400 MHz to 15 GHz, for 13 smaller diameter ‘secondary’ sources whose flux densities were determined by measuring their ratios to Virgo A. Of these 13 sources, three – 3C48, 3C147, and 3C286, are very compact, and have been extensively utilized by the VLA, and other interferometers, for calibration.

Early observations taken by the VLA at 4885 and 1465 MHz suggested that the ratios of the flux densities of 3C48, 3C147, and 3C286 deviated, at the level of a few percent, from ratios derived using the Baars *et al.* (1977) expressions. As some, or all of these sources were known to be variable, a program was started in 1983 to measure the ratios of the flux densities of a set of small-diameter sources, including six of the Baars *et al.* (1977) secondary sources, at a range of frequencies accessible to the VLA. The goals were to correct, where necessary, the Baars *et al.* (1977) expressions for the adopted calibrators (relative to one

or more of them selected as the standard), and to track any temporal variations of their flux densities. As even the smallest of these secondary sources are significantly resolved to the VLA in its highest resolution configurations, most observations in this program were conducted while in the most compact configuration, with maximum spacing of ~ 1 km. This program – modified and expanded as noted below – has continued since 1983.

The majority of scientific observations taken in the 1980s were at the 6-cm and 20-cm receiver bands. Beginning in the later 1980s, and extending into the 1990s, significant improvements in VLA capabilities were implemented as new receiver bands were added, three of the initial four receiver bands were improved, and the technique of referenced pointing was implemented, enabling much more precise high frequency observations. These changes required new calibration objects to be added to this program, and a new flux density reference source, valid for high frequencies, to be used, since the Baars *et al.* (1977) expressions are valid only to 15 GHz.

We will make frequent references in this paper to the VLA’s receiver bands, and to particular frequencies chosen for the observations. The appropriate nomenclature for these bands has long been a matter for debate – the common use of letter band codes, although convenient from the engineering point of view, is not useful, and often confusing for non-radio astronomers, especially since the same letters are often used by other astronomical instruments for completely different frequency bands. In this paper, we will not utilize these letter codes, except where their compactness is required in tables. When we are referring to a particular receiver system, we will refer to it as a frequency band, and denominate it by the wavelength of the central frequency of that band. When we refer to a result which is specific to a chosen frequency, we will denominate it by that frequency. We show in Table 1 the band names, the frequency tuning ranges for each, and the commonly-used letter code.

2. Determining Flux Densities through Interferometry

Single-dish total-power radio telescopes are conceptually simple, but have distinct disadvantages for accurately measuring the flux densities of radio sources, particularly at low frequencies. Their low resolution prevents discrimination against background objects or extended emission located in the primary beam, so the observed power includes unrelated sources whose contributions can only be estimated statistically by observing nearby fields. This problem is particularly severe for sources embedded in a bright extended background such as the galactic plane. By contrast, an interferometer functions as a spatial filter, discriminating against smooth backgrounds, while at the same time, with its higher resolution, enabling separation of the target source from the nearby confusing sources.

The relation between the cross-product spectral power, P_{corr} , provided by an interferometer, and the spectral flux density (or visibility) S of a source is expressed as (Perley (2010)):

$$S = \frac{2k}{\eta_a \eta_e} \frac{1}{\sqrt{\epsilon_1 A_{p1} \epsilon_2 A_{p2}}} \sqrt{\frac{T_{cal1} T_{cal2}}{P_{D1} P_{D2}}} P_{corr}, \quad (1)$$

where η_a is the atmospheric attenuation, η_e is the efficiency of the digital electronics, including the correlator, A_{pn} and ϵ_n are the physical area and aperture efficiency, respectively, of antenna n . Calibration of the electronics, including variations in the gain, is accomplished by utilizing the value, P_D , measured at the correlator, of a signal of power $P_{cal} = kT_{cal}\Delta\nu$ injected at the receiver.

Equation (1) could be used to directly determine the flux density of a source provided all the factors were known with sufficient accuracy. But in fact there are significant uncertainties in the determination of some of these:

- Correction for system gains, and changes in the gains, requires accurate knowledge of the switched power, P_{cal} . These values are measured in the lab, but after deployment

in the field, the actual values may vary by a few percent, due to variations over time and temperature. Furthermore, because the switched power measurement is a true total power measurement, even low levels of radio-frequency interference (RFI) can perturb the measurements of P_D . This is a significant problem for the lower frequency bands.

- The antenna aperture efficiency, ϵ , measures the fraction of the total incident source power intercepted by an antenna which is delivered to the receiver. Factors which reduce efficiency include blockage and refraction of the incoming signal by the support legs and subreflector, the illumination taper introduced by the feed, mispointing of the antenna, errors in optical alignment, and distortions of the primary reflector. In general, the efficiency of the VLA's antennas is known with an accuracy of $\sim 5\%$. The antenna efficiency is a strong function of elevation at the higher frequencies due to gravitationally-induced distortions of the antenna surface and quadrupod support legs.
- The atmospheric absorption term, η_a , has a strong elevation dependency at higher frequencies, and can be time and spatially variable due to clouds.

Because of these uncertainties, direct use of eqn.(1) to convert the interferometer products to flux density has not been practical for the VLA if accuracies better than $\sim 10\%$ are desired. However, provided the system calibration powers are in error by only a constant scale factor, and that the effects of antenna efficiency and atmospheric absorption can be parameterized as time-independent functions of elevation, the VLA can be used to determine highly accurate flux density ratios between calibrators. In the following sections, we demonstrate how ratios with accuracies much better than 1% can be determined at most frequencies, and how these ratios can be used to determine accurate absolute flux densities by using the planet Mars as the reference.

3. The Methodology of Correcting Variable Gains

The major factors which degrade the VLA’s ability to accurately measure flux density ratios are changing system gains, errors in antenna pointing, and elevation dependencies of the antenna gain. In this section, we describe how each can be mitigated through careful observing strategies and data post-processing.

3.1. Accounting for Changing System Gains

To monitor system gains, a small, known amount of noise power is added to the receivers, square-wave modulated at a frequency of 10 Hz. This additional power is synchronously detected and measured at the correlator. Changes in the detected calibration power reflect changes in electronic gains, provided the injected power is itself stable. To demonstrate the effectiveness of this system, we show in Figure 1 the correlation amplitudes (visibilities) for a point source when the gain corrections have, and have not been applied. These data were taken in clear weather over a 40-hour period at a frequency of 4885 MHz, at which the elevation-dependent antenna gain corrections and atmospheric opacity effects are negligible. The application of the switched power correction has reduced the apparent flux density variations from $\sim 50\%$ to less than 1%.

3.2. Correcting for Antenna Pointing

Observations made in the early years of this program clearly indicated that the primary source of error in the gain calibration process at frequencies above ~ 10 GHz is due to offsets in antenna pointing. The accuracy of blind VLA pointing at night under calm conditions is about 10 arcseconds. On sunny days, pointing offsets induced by differential solar heating of the antenna structure can exceed 1 arcminute – larger than the FWHM of the VLA primary

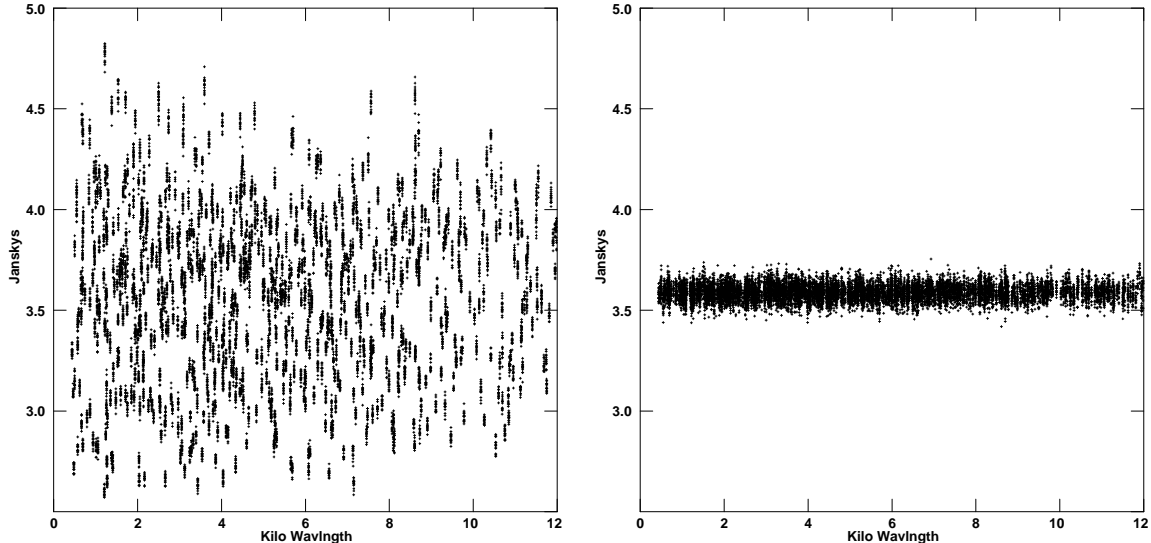


Fig. 1.— The left panel shows the visibilities for the calibrator J0217+7349 without correcting for system gain variations. The right panel shows the visibilities following correction for system gain changes using the switched power monitoring. Both plots are on the same scale to demonstrate the effectiveness of the switched power corrections.

beam at the highest frequency band.

To remove such errors, the method of ‘referenced pointing’ was implemented on the VLA in the mid-1990s (Kestevan (1994)). In this method, a pointing determination is made on a nearby calibrator (or on the target source itself, if sufficiently compact), and the offset correction applied to subsequent observations. Utilization of this technique can reduce pointing error to as low as 3 arcseconds, providing the calibrator object is close enough – ideally within 5 degrees in azimuth and elevation, and preferably less than 15 degrees – and the weather calm and clear. The offset determination is normally made at a frequency within the 3cm band, as this has the best combination of sensitivity and resolution, and the results applied to observations made at other frequency bands. This methodology was first employed in our program in 1995, and was utilized for all following observations.

3.3. Correction for Elevation Gain Dependency

The VLA antennas lose forward gain at high frequencies from a combination of deformation of the antenna surface and a bending of the quadrupod feed leg structure. The loss of gain at high frequencies is significant, but is repeatable and can be corrected for with good accuracy, as illustrated by the fits shown in Figure 2, taken from 43 GHz observations in October, 2011. Referenced pointing was applied to these observations – the scatter

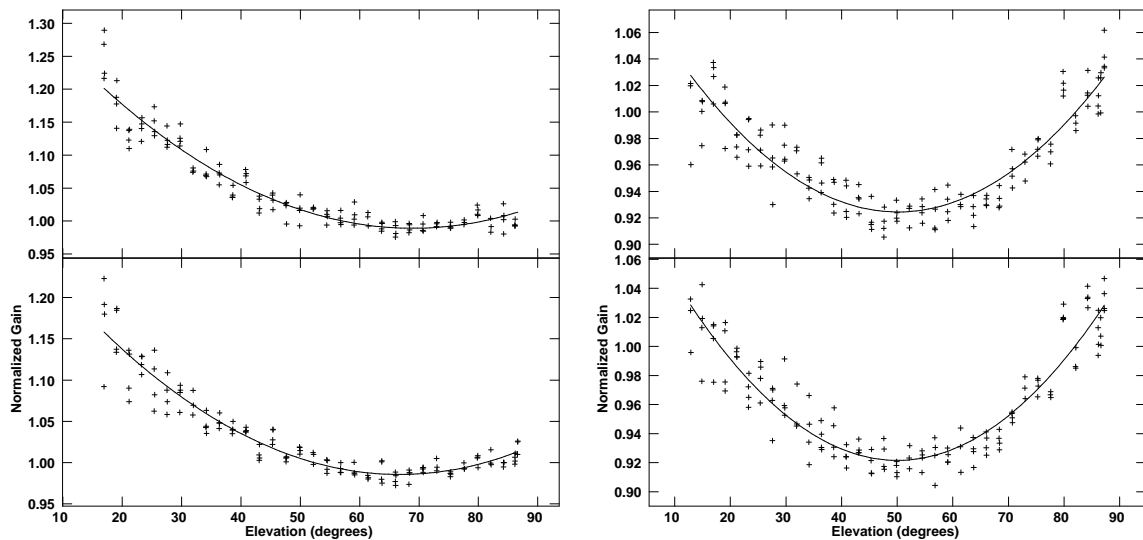


Fig. 2.— Examples of the elevation voltage gain dependencies at 43 GHz. The left panel pair shows the fit for both polarizations for antenna 21, the right panel pair for antenna 23. The post-fit rms power gain residuals are about 3% for both antennas, corresponding to a pointing residual of four arcseconds.

about the best-fit gain represents the current limit for VLA pointing – approximately four arcseconds, rms.

4. Source Selection

The source list for the inaugural June 1983 observations comprised the entire Baars *et al.* (1977) source list, plus the compact source 3C138 which, although known to be variable, is useful for calibration because of its small angular size and high fractional linear polarization. From these, the seven most compact objects were selected for further observations. These were: 3C48, 3C123, 3C138, 3C147, 3C286, 3C295, and NGC7027. These sources were observed in all of the 19 separate observation sessions.

Over time, additional objects were added to the list: 3C196 in 1989, NGC6572 in 2000, and MWC349 in 2001. Beginning in 1995, observations of the planets Mars, Venus, Jupiter, Uranus, and Neptune were added to enable extension of the scale to the highest frequencies utilized by the VLA, since the planets are commonly used as millimeter-wavelength flux density standards (e.g. Griffin and Orton (1993)). Jupiter was dropped from the list after four sessions, as it is too large for its total flux density to be accurately measured by the VLA at the high frequency bands.

We selected the planet Mars as the primary high-frequency standard. Mars is an excellent source for this role, as it has a good emission model (Rudy *et al.* (1987), Muhleman and Berge (1991), Sidher *et al.* (2000)), is usually free of clouds and dust that can affect cm-wavelength observations, and is usually small enough to be only partially resolved to the VLA in its most compact configuration at all frequency bands. The recent publication of the absolute WMAP observations of Mars by Weiland *et al.* (2011) has provided the capability of placing the entire cm-wavelength flux density scale on an absolute standard.

Not all sources were observed at all frequency bands at all sessions, as the planets are too weak to have been detected at frequencies below ~ 5 GHz prior to the VLA's upgrade, and 3C123 is too heavily resolved at the highest frequencies. As the VLA's sensitivity

improved dramatically following the implementation of the WIDAR correlator in March 2010, subsequent observations included Venus, Mars, Uranus and Neptune at all bands except at 90cm.

5. Observations

The observations were made in 19 observing sessions on the dates listed in Table 2. The table also lists the time spent for each session, the configuration in which the observations were made, a summary of the available frequency bands, and a brief note about the weather conditions.

5.1. Frequency Selection

The major goals of this program included both an accurate determination of the variability of the sources, and an accurate determination of the flux density ratios between the sources over as wide a frequency range as possible. As both the VLA's original, and the new WIDAR correlator provide correlation products for two different frequency tunings within each frequency band, we strove to fix one of these tunings to a value which remained unchanged throughout the duration of the project, and to place the other at the maximum separation allowed by the electronics at the time of observing. Due to changes in the VLA's electronics over thirty years, evolution of the goals of the project, and changes in our understanding of the location and impact of RFI, the specific frequencies utilized changed over the observation period, most notably at the lower frequencies. The frequencies chosen for all sessions up to 2006 are given in Table 3.

Major changes in VLA electronics due to the VLA's upgrade permitted a much wider range in frequency selection for sessions after 2006. Observations after this date added

new frequencies, but always retained those listed in the last line of Table 3. The 90cm band observing system was disabled in 2009, so no observations were possible at this band following the 2008 session. Due to the implementation of new receivers, no 2 cm band data were taken in the 2010 session.

5.2. Observing Methodology

The general methodology was to observe each source approximately hourly at each band. To prevent holes in coverage, the durations of most sessions were at least 24 hours. Given the restrictions in antenna slew rate, source separation, and source elevation, we typically obtained five to ten individual ‘snapshot’ observations of each object at each band, with each observation’s duration being 30 to 60 seconds. This methodology permits accurate estimation of and correction for elevation-dependent telescope characteristics, and allows a good estimation of the errors in the flux density. This multiple observation strategy also ensures minimal impact on the project goals in case of short-duration telescope malfunctions, bad weather, and sporadic interference. To permit careful editing of discrepant data, the visibility integration time was kept short, typically 3.3 seconds or less.

5.3. Calibration

All editing, calibration, imaging, and image analysis were done within the AIPS software package (Greisen (2004)). The same editing and calibration methodology was employed for every source at each band for every session, to maximize uniformity and reliability of the results. The sequence of operations was as follows:

1. **Initial editing:** Most sources are strong enough to allow a simple initial editing to purge obviously invalid data – typically showing up as abnormally low amplitudes.

On occasion, RFI or solar interference was seen, with the affected data removed in the same way.

2. **Estimation of atmospheric opacity:** For the observations made between 1995 and 2007, antenna dips were done every six hours at 1.3cm and 0.7cm bands to permit estimation of atmospheric opacity (Butler (1996)). These values, or the values from an atmospheric model using surface and seasonal weather data for the years where no dip data were available (Butler (2002)), were applied to the visibility data.
3. **Removal of atmospheric and instrumental phase perturbations:** Phase fluctuations were removed by application of phase self-calibration for each source, using a point-source model for the unresolved sources, or a ‘clean-component’ model for resolved sources. In the latter case, the model was derived from the data, using an imaging/self-calibration loop. For both, the phase solutions were determined for each time integration, and the results applied to the corresponding visibility data. The SNR for the low-frequency planetary observations was generally too low to permit this procedure – however, at these frequencies, the phase stability was always good enough that such detailed phase fluctuation removal was not necessary.
4. **Removal of data taken with bad pointing:** The most difficult error to detect – and the error which ultimately limits the accuracy of high frequency observing – was that due to residual pointing errors. We did this by first making an amplitude calibration solution for each source, using either a point-source model, or a ‘clean-component’ model. We then examined these solutions, flagging those data for which the corresponding power gains deviated by more than a fixed fraction, varying from 1% for the low frequency bands to 25% for the highest frequency band. In nearly all cases, the flagging is on data whose amplitudes are too low – consistent with the cause being pointing offsets. To prevent bias, all sources at any one band were flagged with

the same threshold. We emphasize that these amplitude gain solutions were never applied to the data – they were utilized only to identify bad data.

5. **Estimation and removal of elevation gain dependency:** The elevation gain dependency was estimated by jointly fitting the calibration gain solutions for the source flux densities and an antenna-based elevation dependency of the form: $G = G_0 + G_1 \sec(z) + G_2 \sec^2(z)$. The resulting gain function was then applied to all the visibility data. For all but the last two sessions, the objects utilized were the four sources which are nearly unresolved at all frequencies in our observations – 3C48, 3C138, 3C147, and 3C286. For the final two sessions, approximately 30 additional point-sources were added to the source list and were included in this calibration step. Separation of the elevation gain dependency from individual pointing offsets required two or three iterations of this and the previous step.
6. **Final gain calibration:** After all discrepant data were removed, and the elevation dependency measured and corrected for, a final amplitude calibration solution was made using a single source, either 3C147 or 3C286. The average gain from these solutions was then applied, without any temporal trend, to all sources in the dataset. Because the primary data products from these observations are the flux density ratios between the sources, the value of the flux density assigned to this source is not important. The only rationale for this final step is one of convenience – to put the source visibilities on a scale close to the correct one.

We made no effort to remove any temporal changes in the amplitude gains, except in the final observing session, which included an additional 30 point sources. These were added for the purpose of investigating the VLA’s gain stability over wide ambient temperature changes. A very small effect was observed at some frequencies, and removed with a 6-hour smoothing window.

5.4. Determination of Flux Density Ratios and Errors

For each source at each session and frequency, the flux density – on the arbitrary scale as noted above – and a likely error were determined with the following procedure – utilized for both unresolved and resolved objects.

- The source flux density was determined from an image utilizing all the data for one session. The image provides two estimates, one from the sum of the clean components, the other from integration over the reconstructed brightness of the source. For sources which were unresolved or marginally resolved, a third estimate from a fit to a 2-D Gaussian profile to the image was made. In all cases, these estimates agreed to within the image noise errors.
- For the four planets, an additional estimation was made from fitting the complex visibility to an appropriate limb-darkened disk model (Butler and Bastian (1999), Butler *et al.* (2001)). A comparison of this estimate to that from the image total flux showed excellent agreement to within the parameter errors generated by the fit.
- An estimate of the error in the derived mean flux density was made from the dispersion of the N individual ‘snapshot’ observations of each source at each band. For each snapshot observation, an estimate of the flux density was made by summing the clean components generated by the deconvolution. The dispersion, σ , was determined from these N estimates, and the error estimate of the mean, σ_μ , was then determined from $\sigma_\mu = \sigma/\sqrt{N-1}$.

This method for determining the measurement error is valid provided the errors in the N observations are statistically independent. We believe this is the case, since the primary source of error in the flux determination at the higher frequencies is from residual pointing errors, which change over a timescale of an hour or less. Furthermore, any residual errors

in the elevation gain dependency correction are likely due to variable atmospheric opacities, which we expect are also variable on time-scales of an hour or less. Since the observations of any individual source are typically separated by an hour or more, we can consider each observation independent of the others.

At low frequencies (90, 20, and 10 cm bands), the errors are dominated by residuals in the deconvolution procedure since the background sources are never perfectly removed, and by errors in the corrections for gain variations. Again, we believe that the characteristic timescale for changes in these errors is typically one hour or less, so that the individual observations are expected to have independent errors.

The primary data products of this program are the flux density ratios between all of the sources. These were determined utilizing the flux densities derived as described above. The errors of these ratios were determined using standard propagation of error methodology, assuming the errors in the flux density of one source are independent of those for the others.

6. Identification of non-variable secondary calibrators

We seek a set of strong, compact, and non-varying objects which can serve as general purpose absolute flux density calibrators. This was done by examining the changes in the ratios of the flux densities of our ten non-planetary target objects over the duration of this project. Since it is extremely unlikely that variability in any one object is correlated over both time and frequency with variability with any other, a constant ratio between two sources over the duration of this project is a strong indicator that both are constant in time. This procedure has the advantage of being independent of the flux density scale imposed by the calibration procedure described above. This analysis was done at the frequencies shown in Table 3 at which our observations spanned the longest period of time: 327.5, 1275, 1465,

4535, 4885, 8435, 8735, 14965, 22460, and 43340 MHz. For some of the sessions, where a particular frequency was not utilized, such as in 1995 and 1998, when 1475 MHz was tuned instead of 1465 MHz, the two frequencies actually tuned within that same band were used, and the desired value derived by a linear interpolation.

This examination showed that the four sources 3C123, 3C196, 3C286, and 3C295, showed negligible changes in their flux density ratios over the duration of this project, and hence should serve as good absolute flux density sources. Plots of the ratios of three of these sources over time are shown in Fig 3. The error bars are $1\text{-}\sigma$ probable errors derived from the estimated errors in the individual flux densities. The red lines are from a weighted linear regression fit. The slopes of the fits, in percent/century, their errors, and the reduced χ^2 of the weighted fits are shown in Table 4. The fitted values of the flux density ratios for the year 2000, and the estimated errors of this ratio are shown in Table 5.

The results of this analysis show that secular changes in the flux densities of these four objects are less than 1% over the 30-year duration of this project, with the exception of the highest frequencies, where the errors limit the accuracy to a few times higher than this.

The unchanging ratio between 3C286 and 3C295 is physically reasonable. VLBI observations of 3C286 show that there is no identifiable inverted spectrum core, and VLBA and EVN polarimetric images (Cotton *et al.* (1997b), Jiang *et al.* (1996)) show a uniform polarization throughout the source’s structure. With no visible compact core, and no detected source expansion, time variability must be of order the light-travel time across the source – hundreds of years for 3C286. As discussed in Ott *et al.* (1994), no variation in 3C295 is expected due to its large physical size (~ 5 kpc) and absence of a significant nuclear core (Taylor and Perley (1992)).

7. Converting Ratios to Absolute Flux Densities

The procedures described above provided ratios between the observed sources accurate to better than 1% at all but the highest frequency band. Conversion of these ratios to absolute flux densities requires at least one source whose absolute flux density is known. We utilize emission models of the planet Mars, combined with absolute measurements of its emission from WMAP, for this purpose, following the procedures described below.

7.1. The Rudy Model Fit to WMAP observations

The flux density of Mars is variable as a function of time, due to both geometrical factors (distance, and subearth latitude and longitude) and to seasonal factors (because of the waxing and waning of the polar caps). It is thus necessary to use a thermophysical model to calculate the expected emission from the planet. Such thermophysical models exist, for example those of Wright (1976) and Rudy *et al.* (1987). We choose to use the latter model (Rudy *et al.* (1987), Muhleman and Berge (1991), Sidher *et al.* (2000)), because it is based on observations at centimeter wavelengths which overlap those of the WMAP measurements, which are absolute (Weiland *et al.* (2011)), as they are calibrated against the CMB dipole.

WMAP measured the brightness temperature of Mars at five frequencies (22.85 GHz (K-band); 33.11 GHz (Ka-band); 40.82 GHz (Q-band); 60.85 GHz (V-band); and at 93.32 GHz (W-band)) during seven ‘seasons’ of observing (Weiland *et al.* (2011)). Three of these frequency bands overlap those available at the VLA, thus providing a good way to transfer the WMAP flux density scale to the higher frequencies of the VLA. By utilizing the thermophysical emission model described above, and incorporating lower-frequency observations described in Baars *et al.* (1977), the entire radio frequency spectrum from ~ 1

GHz to 50 GHz can be placed on an absolute calibration scale.

The spectral flux density measured by a total power telescope such as WMAP for any particular pointing is the antenna beam-weighted integral of the sky brightness over the full sky:

$$S = \int BPd\Omega \quad (2)$$

where B is the sky brightness, P is the normalized antenna power pattern, and the integration is over 4π steradians. The *increment* in spectral flux density, S_p , provided by a uniform, discrete source of solid angle Ω_p (assumed much smaller than the antenna main beam), brightness B_p and opacity τ , – hence the value actually measured by the telescope – is

$$S_p = [B_p - B_{bg}(1 - e^{-\tau})]\Omega_p. \quad (3)$$

where B_{bg} is the sky brightness behind the foreground object. The second term on the right-hand side accounts for the attenuation of the background sky by the source. For an optically thick source, such as a planet, this becomes

$$S_p = (B_p - B_{bg})\Omega_p. \quad (4)$$

Thus, flux density measured by the telescope is proportional to the brightness difference between the object and the background sky. To this value must be added that amount occulted by the object in order to determine the actual flux density. These considerations apply equally to interferometers, as the uniform background sky is resolved out by the interferometric coherence pattern.

For our application, both the planet brightness B_p and the background sky brightness B_{bg} are described by the Planck function

$$B(\nu, T) = \frac{2h\nu^3}{c^2} \frac{1}{e^{h\nu/kT} - 1} \quad (5)$$

where T is the brightness temperature of the source. The WMAP brightness temperatures of Mars published in Weiland *et al.* (2011) are given in terms of the ‘Rayleigh-Jeans’ brightness temperature, defined as

$$T_{RJ} = \frac{\lambda^2 S_\nu}{2k\Omega}, \quad (6)$$

and have not been adjusted by the blockage of the sky background. Since the Rudy model provides an estimate of the total brightness of the source in true ‘Planck’ units, we must adjust the published WMAP values for both the blockage and the difference in units.

From equations 5, 6, and 7, we can relate the true brightness temperature of an optically thick object, T_P , to the value assigned using the Rayleigh-Jeans approximation, T_{RJ} , accounting for the flux blocked by the planet’s disk:

$$\frac{h\nu}{kT_P} = \ln \left[1 + \frac{1}{(e^{h\nu/kT_{bg}} - 1)^{-1} + \frac{kT_{RJ}}{h\nu}} \right] \quad (7)$$

With $T_{bg} = 2.75K$, we find that the published WMAP values for Mars must be increased by 2.78, 2.82, 2.86, 3.00, and 3.32 K for the five frequency bands used by WMAP. The WMAP observations of the brightness temperature of Mars for all frequencies and sessions are shown in Table 6, along with the values adjusted as described above.

Given the WMAP observation dates, we then calculate the Rudy Model brightness temperatures for each observation, averaged over a full rotation of Mars, since the Rudy Model has variations as a function of planetary longitude, based on surface thermophysical properties, and the Weiland *et al.* (2011) results do not include a time of day of the observations. The Rudy Model values calculated in this way are also shown in Table 6. Figure 4 shows the fits along with the model calculations for all five bands.

With the WMAP observations and the Rudy Model predictions for a given frequency, we then find a correction factor to apply to the Rudy Model to make the best agreement

with the WMAP observations, given by:

$$f = \frac{\sum w_i M_i D_i}{\sum w_i M_i^2} \quad (8)$$

where the M_i are the Rudy Model values, D_i the WMAP observed values, and w_i the WMAP weights ($w_i = 1/\sigma^2$).

Table 7 shows the derived corrections at each band, and an error estimated from the dispersion in the individual ratios – for these estimates we did not use the ‘season 1’ WMAP observations in this fit, since they were taken during a global dust storm (Weiland *et al.* (2011)). These storms are known to change the planet’s emission, and are not included in the model.

We find little evidence of the unmodeled frequency dependent emissivity reported by Weiland *et al.* (2011); what they reported may have been a byproduct of their extrapolation of the Wright Model to inappropriate frequencies. Because we find no strong evidence for variation of the correction factor across these five bands, we have applied the average correction factor of 0.975 from the lowest three WMAP frequencies to the spectral flux densities derived from the Rudy model.

7.2. Generating the Apparent Flux Density of Mars

The Rudy model calculates the *total* spectral flux density from the planet Mars. To determine that actually measured by the VLA requires subtracting that portion blocked by the planet’s disk, as described in Section 7.1. The background brightness temperature T_{bg} is

$$T_{bg} = T_{gal} + T_{cmb}. \quad (9)$$

where $T_{cmb} = 2.725$ K and T_{gal} is the brightness temperature of the galactic background. This is widely variable, depending on galactic longitude and latitude. For our observations,

Mars was always sufficiently far from the galactic plane that we can utilize the expression $T_{gal} \sim 2.5\nu_G^{-2.7}$ K, where ν_G is the frequency in GHz, to estimate the galactic contribution. In general, the galactic synchrotron brightness is negligible compared to the CMB at frequencies above 2 GHz. For observations below 2 GHz, the galactic background can contribute a small offset, but this is completely negligible compared to the errors in the observations due to the low flux density of Mars below 2 GHz.

The results of this procedure are shown in Table 8, giving the apparent flux density of Mars for the dates, times, and frequencies shown. Also shown are the approximate coordinates, in equatorial and galactic coordinates, of Mars during our observations.

For each observing session and frequency, the ratio between our observed spectral flux density of Mars, based on the arbitrary calibration scale described earlier, and the calculated apparent spectral flux density of Mars shown in Table 8 was used to adjust the derived flux densities of the four non-varying sources 3C123, 3C196, 3C286, and 3C295 to the Mars-based scale. For the 90cm band ratios, where the VLA cannot detect Mars, we have used the Scaife and Heald (2012) value for 3C196 as the reference source.

8. Polynomial Expressions for the Flux Densities of 3C123, 3C196, 3C286, and 3C295

Our derived flux densities for each of the four primary flux density calibrators, based on their ratios to the planet Mars and utilizing the Rudy Model adjusted to the WMAP scale are given in Table 9. The values listed at 327.5 MHz – where Mars is too weak to be detected – are based on our measured ratios to the source 3C196, whose spectral flux density is set to the Scaife and Heald (2012) value of 46.75 Jy. We emphasize that the Scaife and Heald (2012) scale is not independently based on an absolute standard, but

utilizes various published observations from the literature which are then tied to a proposed common flux density scale. We include these low frequency values to our fits in order to provide a plausible low-frequency extension of our proposed scale.

The listed errors shown in Table 9 are estimated from the dispersion in the measurements of the individual ratios to Mars taken since 1995. The number of separate observations for each band is given in the right-hand most column.

Table 1. VLA Frequency Band Nomenclature

Band Name	Band Code	Frequency Range (MHz)
90cm	P	300 – 340 ^a
20cm	L	1000 – 2000
10cm	S	2000 – 4000
5cm	C	4000 – 8000
3cm	X	8000 – 12000
2cm	Ku	12000 – 18000
1.3cm	K	18000 – 26500
0.9cm	Ka	26500 – 40000
0.7cm	Q	40000 – 50000

^aThis is the tuning range of the old 90cm band system which was disabled in 2009. The VLA is currently being outfitted with a new 90cm receiver system which spans 270 to 400 MHz.

Table 2. Observing Log

Date	IAT Start	LST Start	Duration	Total	Configuration	Bands	Comments
02-03 Jun 1983	22:30	07:50	25	25	D	LCKuK	Clear
28-29 Dec 1985	02:50	02:00	22	22	D	PLCKuK	Clear
04-05 May 1987	07:45	15:20	24	24	D	PLCCKuK	Clear, calm
29-30 Dec 1989	09:40	09:00	23	23	D	PLCCKuK	Cloudy
09 Jul 1992	07:35	19:39	13	13	D	PLCCKuK	Cloudy
26 Aug 1992	01:25	16:30	5	5	D	PLCCKuK	T-storms
13-14 Mar 1995	21:50	02:00	24	24	D	PLCCKuKQ	Partly cloudy
03-04 Feb 1998	12:20	14:00	28	28	D	PLCCKuKQ	Cloudy, light snow
15-16 Apr 1999	23:10	05:35	24	24	D	PLCCKuKQ	Clear
02-03 Oct 2000	22:55	16:30	24	24	D	PLCCKuKQ	Clear
09-10 Nov 2001	23:55	20:10	25	25	D	PLCCKuKQ	Partly cloudy
06-07 Feb 2003	19:40	21:35	30	30	D	PLCCKuKQ	Mostly clear
27-30 Aug 2004	01:30	16:35	27	34	D	PLCCKuKQ	Mostly clear
15-20 Jan 2006	23:00	23:30	29	45	D	PLCCKuKQ	Windy
13-14 May 2007	13:00	22:10	31	31	D	PLCCKuKQ	Clear
11-15 Sep 2008	01:30	18:00	44	106	D	PLCCKuKQ	Mostly clear
09-11 Jan 2010	08:50	09:00	31	36	D	LSCCKKaQ	Clear
26-27 Dec 2010	16:30	15:45	30	30	C	LSCCKKuKKaQ	Clear
19-20 Jan 2012	00:30	01:10	30	31	DnC	LSCCKKuKKaQ	Clear, Breezy

Note. — The durations column gives the length of the scheduled observing run in hours. For some sessions, additional observing time was obtained within a few days of the primary block, as reflected by the difference between the Durations and Total columns. Band names are coded for brevity: P=90cm, L=20cm, S=10cm, C=6cm, X=3cm, Ku=2cm, K=1.3cm, Ka=0.9cm, Q=0.7cm. The longest baseline in D configuration is ~ 1 km, and ~ 3 km in C configuration.

Table 3. Detailed Frequency Settings, in MHz, from 1983 through 2006

Year	P1	P2	L1	L2	C1	C2	X1	X2	U1	U2	K1	K2	Q1	Q2
1983				1465		4885				14965		22485		
1985	317	333	1425	1465	4835	4885			14915	14965	22435	22485		
1987	327	333	1425	1465	4816	4866	8435	8485	14934	14984	22435	22485		
1989	327	333	1425	1465	4816	4866	8435	8485	14934	14984	22435	22485		
1992	327	333	1425	1465	4816	4866	8435	8485	14934	14984	22435	22485		
1995	327	333	1365	1475	4835	4885	8415	8465	14915	14965	22435	22485	43315	43365
1998	321	327	1365	1475	4835	4885	8435	8485	14915	14965	22435	22485	43315	43365
1999	321	327	1275	1465	4835	4885	8435	8485	14915	14965	22435	22485	43315	43365
2000-2006	321	327	1275	1465	4535	4885	8435	8735	14915	14965	22435	22485	43315	43365

Note. — Additional frequencies were added in the 2007 and 2008 sessions to allow more uniform spectral coverage. Frequency selections for the wideband WIDAR correlator (sessions 2011 and 2012) were set to include the frequencies shown in the last row of the table. No 90cm band observations were made after the 2008 session, nor in the 2cm band in 2010, due to EVLA construction.

Table 4. Secular Changes in Flux Density Ratios amongst Three Sources

Freq. MHz	286/295 %/century	χ^2	196/286 %/century	χ^2	196/295 %/century	χ^2	123/196 %/century	χ^2	123/286 %/century	χ^2	123/295 %/century	χ^2
327.5	1.6±2.4	1.2	10.3±3.2	4.0	11.4±2.6	7.0	-0.1±2.5	1.4	9.8±2.7	5.9	13.3±2.7	9.8
1275	2.2±1.7	9.8	1.8±1.8	7.6	3.2±1.6	0.2	-5.3±3.2	3.3	3.7±3.5	20	-2.4±3.5	3.1
1465	1.1±0.3	1.6	-1.3±0.5	2.4	-1.2±0.5	3.2	-1.1±0.9	1.3	-0.4±0.6	8.7	0.3±0.5	2.3
4535	-3.2±1.3	1.8	-0.3±1.3	3.2	-3.6±1.1	3.9	-0.8±1.1	6.1	2.2±1.4	4.2	-7.3±1.0	8.7
4885	1.7±0.2	3.2	-1.6±0.5	3.0	-0.5±0.7	5.5	-0.8±1.0	2.9	0.2±0.9	3.9	-0.3±0.9	7.4
8435	0.2±0.4	1.5	3.2±0.9	1.3	1.0±0.8	1.7	-3.9±1.1	3.5	-1.7±1.1	7.4	-2.8±0.9	7.3
8735	-1.2±0.8	0.5	3.1±1.1	3.3	1.2±0.9	1.4	-2.4±1.1	3.7	1.5±1.0	10	-1.5±1.1	6.0
14965	-1.7±1.4	1.1	7.8±2.2	3.0	6.6±2.3	4.4	-12 ±3.1	2.7	-2.8±3.3	2.2	-6.0±3.2	3.3
22460	-4.8±1.5	1.1	17±3.6	2.1	4.8±3.8	2.2	-11 ±5.6	4.4	6.5±5.9	3.7	-7.5±6.5	1.5
43340	4.8±9.5	1.4	43±15	1.1	40±17	0.9	-61 ±94	2.2	-11±102	0.1	-41±102	0.0

Note. — Listed are the linear rate of change in flux density ratio amongst three of the four apparently constant sources, in percent/century, along with the estimated error of this slope and reduced χ^2 of a weighted fit.

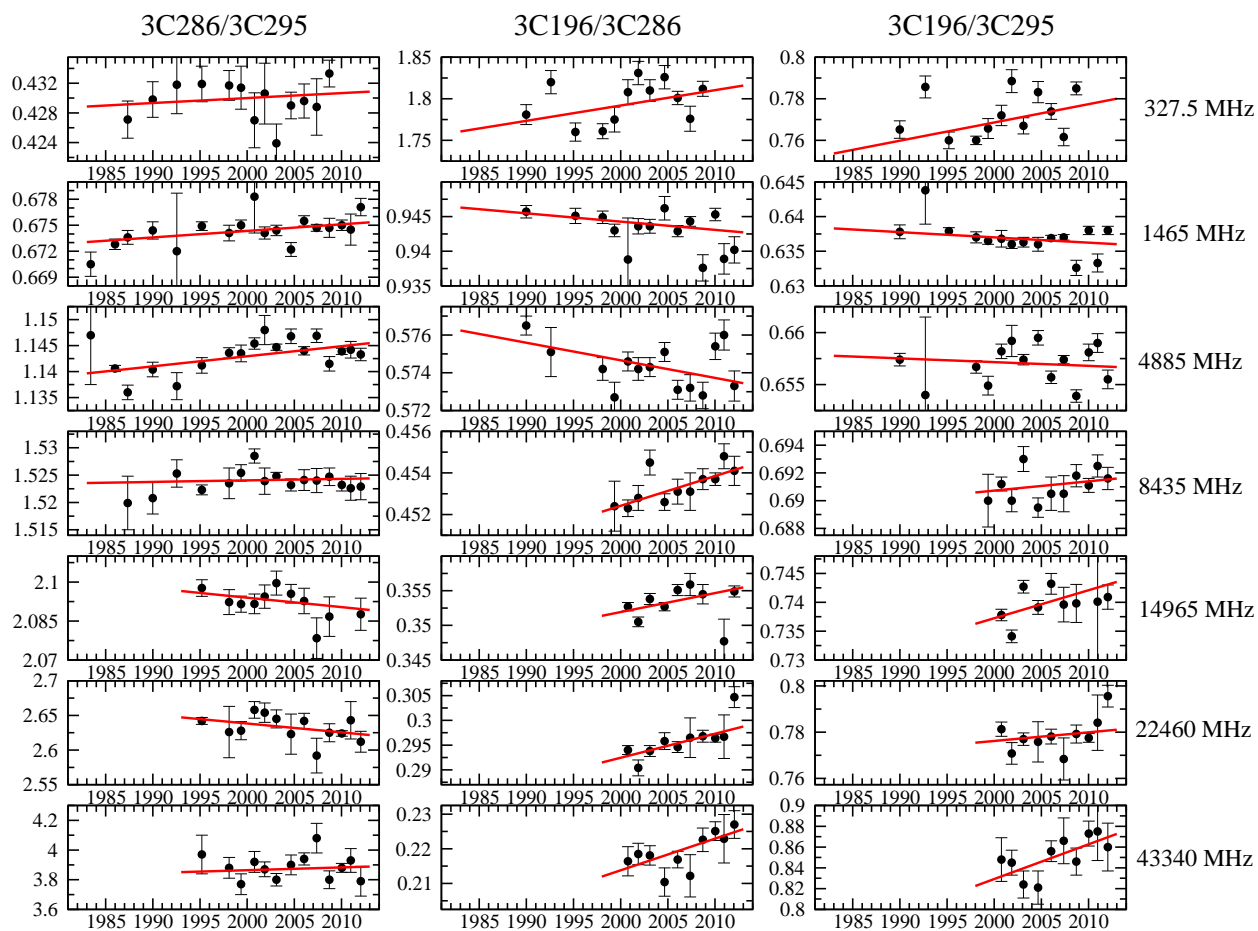


Fig. 3.— Showing the ratios of the flux densities between 3C286, 3C196, and 3C295, as a function of time and for selected frequencies. Secular changes are very small, typically a few percent/century, except at the highest and lowest frequencies, where the errors are highest. The red lines show a weighted linear regression fit.

Table 5. Flux Density Ratios for date 2000.0 for the Four Primary Sources

Freq.	R(286/295)	R(196/286)	R(196/295)	R(123/196)	R(123/286)	R(123/295)
327.5	0.4299±0.0007	1.7919±0.0034	0.7686±0.0011	3.1012±0.0050	5.5688±0.0100	2.3990±0.0035
1275	0.6435±0.0006	0.9943±0.0010	0.6399±0.0006	3.3565±0.0043	3.3215±0.0050	2.1482±0.0031
1465	0.6743±0.0002	0.9443±0.0003	0.6370±0.0002	3.3872±0.0014	3.1923±0.0010	2.1554±0.0006
4535	1.1041±0.0008	0.5929±0.0004	0.6541±0.0004	3.7671±0.0023	2.2339±0.0016	2.4688±0.0014
4885	1.1430±0.0002	0.5747±0.0002	0.6572±0.0003	3.7945±0.0019	2.1772±0.0010	2.4918±0.0012
8435	1.5240±0.0004	0.4524±0.0003	0.6907±0.0004	4.0188±0.0026	1.8210±0.0013	2.7782±0.0017
8735	1.5551±0.0009	0.4456±0.0003	0.6935±0.0004	4.0288±0.0023	1.7944±0.0009	2.7944±0.0017
14965	2.0940±0.0014	0.3519±0.0004	0.7372±0.0008	4.2670±0.0052	1.5022±0.0024	3.1496±0.0041
22460	2.6383±0.0031	0.2924±0.0007	0.7762±0.0023	4.4526±0.0139	1.3033±0.0046	3.4551±0.0026
43340	3.864 ±0.026	0.2138±0.0022	0.829 ±0.010	4.5 ±0.5	0.93±0.10	3.7±0.4

Note. — The ratio values at 43.3 GHz involving 3C123 are of much poorer quality due to the large angular size of that source.

Table 6. WMAP Observations and Rudy Model Data

JD	22.85 GHz			33.11 GHz			40.82 GHz			60.85 GHz			93.32 GHz		
	W	C	M	W	C	M	W	C	M	W	C	M	W	C	M
2182.62	178±4	181	195	182±3	185	195	186±4	189	195	191±3	194	196	189±2	192	196
2776.39	183±4	186	194	187±3	190	196	191±4	194	198	197±3	200	202	204±2	207	206
2983.75	191±4	194	200	195±3	198	200	185±4	188	201	193±3	196	201	195±2	198	202
3586.17	200±3	203	207	199±2	202	210	203±3	205	212	209±2	212	215	213±1	216	220
3758.26	191±5	194	190	184±3	187	190	189±4	192	190	186±3	189	190	185±2	188	192
4389.29	186±4	189	196	187±3	190	198	196±4	199	199	197±3	200	203	198±2	201	207
4530.49	174±6	177	184	177±4	180	184	176±5	179	184	181±4	184	185	182±2	185	186

Note. — For each WMAP observing band is listed the published WMAP brightness temperature (‘W’), the temperature after correction for the sky background and conversion to Planck units (‘C’), and the Rudy model prediction (‘M’). The listed JD date has had 2450000 subtracted.

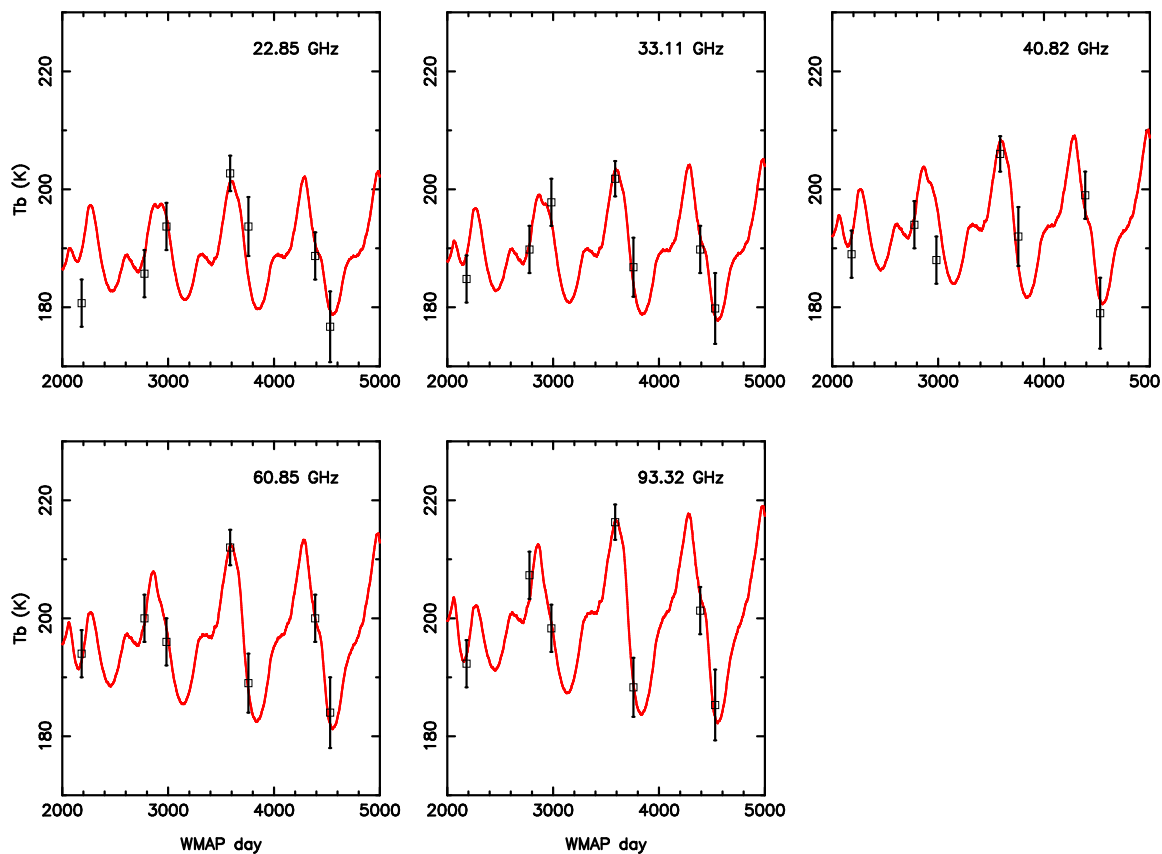


Fig. 4.— The red line shows the predictions of the adjusted Rudy model to the WMAP observations, shown as the black data points. The regular oscillations are due to a combination of orbital motions of the Earth and Mars, the inclination of Mars, and Martian seasonal variations.

Table 7. Rudy Model Correction Factors for Agreement with WMAP Data

	K	Ka	Q	V	W
Ratio	0.974	0.970	0.985	0.987	0.987
Error	0.008	0.005	0.011	0.003	0.005

Table 8. Calculated Apparent Mars Spectral Flux Densities at Selected Frequencies

Date	α hh mm	δ sdd mm	l ddd	m sdd	Dist. AU	Diam. arcsec.	1465 MHz	4885 MHz	8435 MHz	14965 MHz	22460 MHz	43340 MHz
1995 Mar 14	09 10	20 18	208	39	0.77	12.1					7.47	27.7
1998 Feb 03	22 37	-09 44	55	-54	2.24	4.2				0.428	0.973	3.68
1999 Apr 16	14 21	-12 19	335	45	0.60	15.6	.0531	0.599	1.79	5.67	12.8	47.9
2000 Oct 03	10 49	08 52	239	56	2.45	3.8		0.0356	0.107	0.335	0.765	2.89
2001 Nov 10	20 50	-19 39	27	-35	1.13	8.3		0.173	0.521	1.65	3.72	13.8
2003 Feb 07	16 49	-22 08	358	14	1.72	5.4		0.0723	0.216	0.686	1.56	5.92
2004 Aug 27	10 50	08 33	240	56	2.66	3.5		0.0301	0.0901	0.285	0.646	2.43
2006 Jan 17	00 52	18 16	123	-45	0.92	10.2	.0234	0.263	0.771	2.414	5.40	20.0
2007 May 14	23 59	-01 43	94	-62	1.71	5.5		0.0747	0.227	0.726	1.66	6.32
2008 Sep 14	13 02	-06 15	308	56	2.45	3.8		0.0355	0.106	0.336	0.773	2.85
2010 Jan 11	09 20	19 55	210	41	0.69	13.5	.0395	0.442	1.32		9.43	35.3
2010 Dec 26	19 01	-23 39	13	-13	2.38	3.9		0.0384	0.116	0.368	0.839	3.17
2012 Jan 19	11 39	06 03	260	63	0.88	10.6	.0243	0.272	0.812	2.57	5.82	21.9

Note. — The spectral flux densities in Jy of Mars, adjusted for background sky brightness, visible to the VLA. Values listed are averages over each session. Missing entries correspond to dates when Mars was not observed, or not detected. Values listed have been adjusted for the attenuation due to the VLA’s primary beam.

Table 9. Adopted Spectral Flux Densities of Steady Sources

Freq. (MHz)	3C123		3C196		3C286		3C295		N_{obs}
	S(Jy)	σ (Jy)	S(Jy)	σ (Jy)	S(Jy)	σ (Jy)	S(Jy)	σ (Jy)	
0.3275	145.0	4.3	46.8	1.4	26.1	0.8	60.8	1.8	14
1.015	66.2	4.3	20.1	4.8	18.4	4.3	30.8	7.3	1
1.275	46.6	3.2	13.3	2.0	13.8	2.0	21.5	3.0	1
1.465	47.8	0.5	14.1	0.2	15.0	0.2	22.2	0.5	4
1.865	38.7	0.6	11.3	0.2	13.2	0.2	17.9	0.3	2
2.565	28.9	0.3	8.16	0.1	10.9	0.2	12.8	0.2	2
3.565	21.4	0.8	6.22	0.2	9.5	0.1	9.62	0.2	3
4.535	16.9	0.2	4.55	.06	7.68	0.1	6.96	.09	7
4.835	16.0	0.2	4.22	.1	7.33	0.2	6.45	.15	1
4.885	15.88	0.1	4.189	.025	7.297	.046	6.37	.04	11
6.135	12.81	.15	3.318	.05	6.49	.15	4.99	.05	2
6.885	11.20	.14	2.85	.05	5.75	.05	4.21	.05	3
7.465	11.01	.2	2.79	.05	5.70	.10	4.13	.07	1
8.435	9.20	.04	2.294	.010	5.059	.021	3.319	.014	11
8.485	9.10	.15	2.275	.03	5.045	.07	3.295	.05	1
8.735	8.86	.05	2.202	.011	4.930	.024	3.173	.016	10
11.06	6.73	.15	1.64	.03	4.053	0.08	2.204	.05	1
12.890			1.388	.025	3.662	.070	1.904	.04	1
14.635	5.34	.05	1.255	.020	3.509	.040	1.694	.04	1
14.715	5.02	.05	1.206	.020	3.375	.040	1.630	.03	1
14.915	5.132	.025	1.207	.004	3.399	.016	1.626	.008	7
14.965	5.092	.028	1.198	.007	3.387	.015	1.617	.007	11
17.422	4.272	.07	0.988	.02	2.980	.04	1.311	.025	1
18.230			0.932	.020	2.860	.045	1.222	.05	1
18.485	4.090	.055	0.947	.015	2.925	.045	1.256	.020	1
18.585	3.934	.055	0.926	.015	2.880	.04	1.221	.015	1
20.485	3.586	.055	0.820	.010	2.731	.05	1.089	.015	1
22.460	3.297	.022	0.745	.003	2.505	.016	0.952	.005	13
22.835	3.334	.06	0.760	.010	2.562	.05	0.967	.015	1
24.450	2.867	.03	0.657	.017	2.387	.03	0.861	.020	2
25.836	2.697	.06	0.620	.017	2.181	.06	0.770	.02	1

The frequency dependencies of the spectral flux densities for the four stable sources were modelled with a cubic polynomial function of the form

$$\log(S) = a_0 + a_1 \log(\nu_G) + a_2[\log(\nu_G)]^2 + a_3[\log(\nu_G)]^3 \quad (10)$$

where S is the spectral flux density in Jy, and ν_G is the frequency in GHz. Because our values for frequencies below 4 GHz have much higher errors, and to enable a plausible low-frequency extension of our scale, we have added the Baars *et al.* (1977) values for 3C123, 3C286, and 3C295 at 0.5, 0.75, 1.0, 2.0, and 3.0 GHz, with the errors given in their paper. The resulting coefficients are given in Table 10, along with the estimated errors of these coefficients. The adopted spectral flux densities, including the Baars values, and the derived fits, for the four steady objects are shown in Fig. 5.

Amongst the four sources, 3C286 is the most compact and has the flattest spectral index, making it the preferred primary flux density reference source. We thus adopt 3C286 as our reference source, and determine the flux densities of all other sources in our program from their ratios to it.

9. Estimated Error in the Scale

There are several sources of error in the measurement and transfer process. Here we quantify these.

1. The intrinsic error in the WMAP brightness scale. This is based on the knowledge of the CMB monopole, given by Jarosik *et al.* (2001) as 0.2%.
2. The error in the correction factor which adjusts the Rudy model to the WMAP scale. We estimate this from the dispersion in the ratios between the Rudy model predictions and the actual WMAP observations. The dispersion in this ratio for the

Table 9—Continued

Freq. (MHz)	3C123		3C196		3C286		3C295		N_{obs}
	S(Jy)	σ (Jy)	S(Jy)	σ (Jy)	S(Jy)	σ (Jy)	S(Jy)	σ (Jy)	
26.485	2.716	.05	0.607	.017	2.247	.05	0.779	.020	1
28.450	2.436	.06	0.568	.015	2.079	.05	0.689	.020	2
29.735	2.453	.05	0.529	.015	2.011	.05	0.653	.020	1
36.435	1.841	.17	0.408	.005	1.684	.02	0.484	.015	3
43.065			0.367	.015	1.658	.08	0.442	.020	1
43.340	1.421	.055	0.342	.005	1.543	.024	0.398	.006	13
48.350	1.269	.12	0.289	.005	1.449	.04	0.359	.013	4
48.565			0.272	.015	1.465	.1	0.325	.025	1

Note. — The derived flux density values, based on the Mars emission model for frequencies between 1 and 50 GHz. The quoted errors are derived from the dispersion of the values over the various sessions. The values for 3C123, 3C286, and 3C295 at 327.5 MHz are derived from their ratios to 3C196, whose flux density is taken to be 46.8 Jy (Scaife and Heald (2012)).

Table 10. Fitted Coefficients for the Four Steady Sources

Source	a_0	a_1	a_2	a_3	χ^2
3C123	1.8077±0.0036	-0.8018±0.0081	-0.1157±0.0047	0	2.01
3C196	1.2969±0.0040	-0.8690±0.0114	-0.1788±0.0150	0.0305±0.0063	2.09
3C286	1.2515±0.0048	-0.4605±0.0163	-0.1715±0.0208	0.0336±0.0082	1.22
3C295	1.4866±0.0036	-0.7871±0.0110	-0.3440±0.0160	0.0749±0.0070	1.65

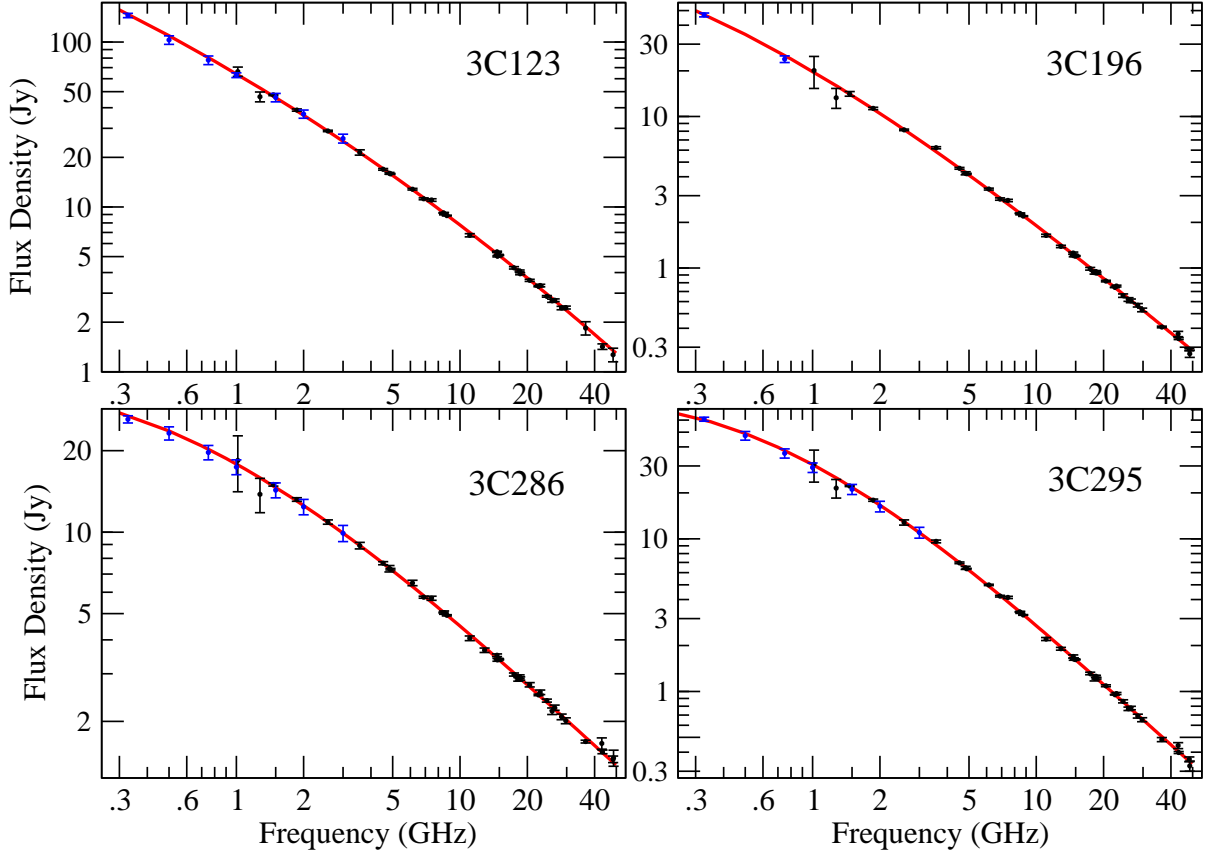


Fig. 5.— Plotted are the measurements of the flux densities, and their $1\text{-}\sigma$ errors for the four non-variable sources, and the best-fit models for each. Data based on the Mars model are plotted in black. Data based on the Baars scale, or the Scaife and Heald (2012) scale are plotted in blue.

18 separate observations at 22.85, 33.11, and 40.82 GHz (excluding the first epoch) is 0.019. Presuming each is independent, the error in the mean is 0.5%.

3. An additional error at low frequencies, where we cannot use WMAP observations to directly correct the Rudy model, but rather rely on the physics of the model properly accounting for the frequency dependence of the emission. Fortunately, the Rudy model is best constrained at those frequencies, since it is based on VLA observations at 5 and 15 GHz. We estimate this error as 1%, based on runs of the model with

varying physical parameters, and consideration of unmodeled effects (see also the discussion in Muhleman and Berge (1991).

4. The error in the transfer from the Mars flux density to that of our chosen standard source, 3C286. This is given by the error in our ratio measurements, as shown in Table 9. We estimate this error as 2% at 1465 MHz, 0.7% at 4885 MHz, 0.5% at 8435 and 14965 MHz, rising to 1% at 22460 MHz, and 2% at 43340 MHz.

Presuming that these four error sources are independent, the total error is given by adding all four in quadrature – roughly 2.5% at 1500 MHz, 1% from 4000 through 15000 MHz, 2% at 22000 MHz, and 3% at 43000 GHz.

10. Spectral Flux Densities and Structures of the Remaining Target Sources

The adoption of 3C286 as the primary flux density standard permits derivation of the spectral flux densities, as a function of frequency and time, for the remaining sources in our program. Here we show the results for the non-planetary target sources.

10.1. 3C48

3C48 is a compact steep-spectrum quasar at redshift $z=0.367$. Its radio structure is quite compact with a maximum extent of about 1.2 arcseconds, as shown by the 0.1 arcsecond resolution VLA image shown in Fig. 6. The brightest regions of this source have been imaged by VLBA, MERLIN, and EVN observations (An *et al.* (2009)). The source is a commonly-used flux density calibration source for the VLA. The plots in the right panel of Fig. 6 show that the source has undergone significant changes in flux density over the past 30 years. A period of slow decline or quiescence was followed by a small flare, more

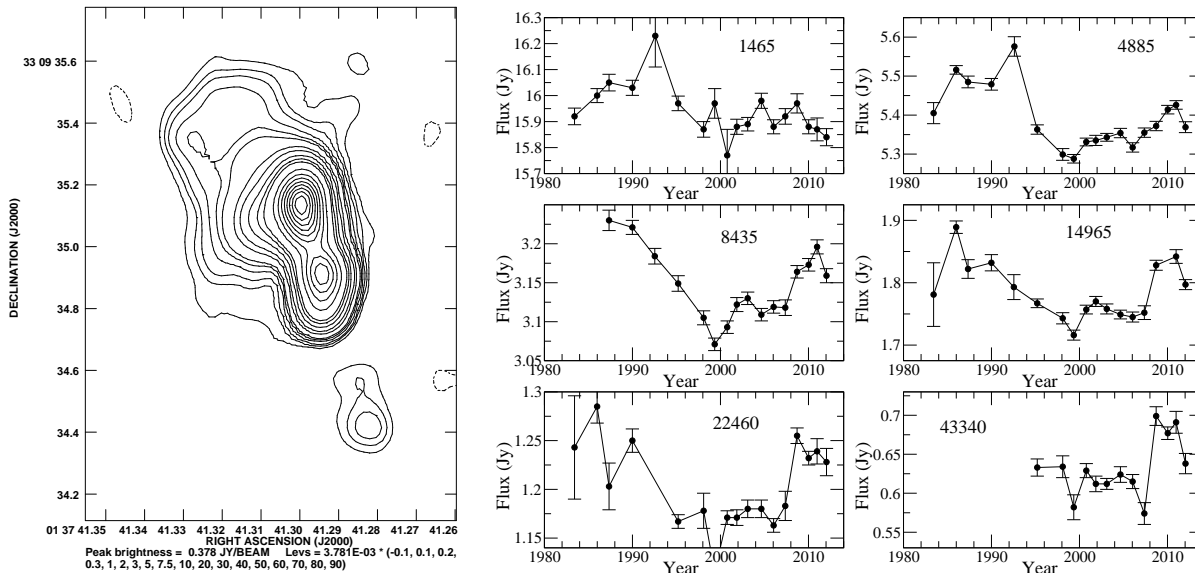


Fig. 6.— The left panel shows the structure of 3C48 at 22.5 GHz, with 100 milliarcsecond resolution. The active nucleus of the quasar is identified with the lower of the two bright peaks. The right panel shows the temporal evolution of the source flux density.

prominent at the higher frequencies, beginning in 2009, which is now declining. As this source is a commonly utilized flux density calibration source, we have fitted its changing spectrum with a cubic polynomial fit for each of the 18 sessions. The results of this are given in Table 11.

10.2. 3C123

3C123 is a radio galaxy at redshift $z=0.218$. With an angular size of 44 arcseconds, it is the largest of the objects in this study, and is of limited use for the calibration of high-resolution interferometers. We included it in this program primarily because it is a well-known calibrator source at low frequencies. The structure of the source, with 3 arcseconds resolution at 22.5 GHz, utilizing the data taken in this program, is shown in Fig. 7.

Table 11. Fitted Coefficients for Temporal Change for 3C48, 3C138, and 3C147

Session	3C48				3C138				3C147			
	A0	A1	A2	A3	A0	A1	A2	A3	A0	A1	A2	A3
1983.4	1.3339	-.7643	-.1946	.055	1.0328	-.5523	-.1161	.008	1.4620	-.7085	-.2347	.051
1985.9	1.3350	-.7598	-.1869	.057	1.0337	-.5591	-.1605	.032	1.4648	-.7177	-.2501	.089
1987.3	1.3361	-.7577	-.1905	.048	1.0354	-.5914	-.1032	-.005	1.4624	-.7115	-.2336	.071
1989.9	1.3363	-.7605	-.1965	.057	1.0292	-.5636	-.1857	.052	1.4646	-.7194	-.2532	.092
1995.2	1.3359	-.7673	-.2041	.059	1.0145	-.5466	-.1758	.038	1.4632	-.7121	-.2346	.086
1998.1	1.3342	-.7732	-.2078	.065	1.0259	-.5679	-.1735	.039	1.4641	-.7090	-.2313	.088
1999.3	1.3342	-.7682	-.2097	.056	1.0204	-.5702	-.1636	.030	1.4642	-.7132	-.2424	.082
2000.8	1.3323	-.7654	-.2091	.060	1.0081	-.5077	-.2492	.064	1.4585	-.7086	-.2296	.068
2001.9	1.3342	-.7708	-.2014	.059	1.0196	-.5627	-.1823	.039	1.4636	-.7124	-.2426	.084
2003.1	1.3341	-.7691	-.2006	.057	1.0177	-.5686	-.1591	.029	1.4639	-.7144	-.2453	.082
2004.7	1.3341	-.7641	-.2102	.059	1.0094	-.5003	-.2642	.085	1.4635	-.7112	-.2453	.091
2006.0	1.3335	-.7705	-.2008	.058	1.0181	-.5543	-.1486	.038	1.4631	-.7136	-.2338	.094
2007.4	1.3335	-.7660	-.1982	.051	1.0149	-.5408	-.1174	.012	1.4645	-.7115	-.2378	.084
2008.7	1.3361	-.7700	-.2119	.076	1.0132	-.4941	-.1556	.045	1.4625	-.7112	-.2396	.081
2010.0	1.3334	-.7662	-.1988	.062	1.0230	-.4983	-.1529	.048	1.4623	-.7139	-.2405	.081
2010.9	1.3332	-.7665	-.1980	.064	1.0207	-.5140	-.1626	.058	1.4607	-.7150	-.2372	.077
2012.0	1.3324	-.7690	-.1950	.059	1.0332	-.5608	-.1197	.041	1.4616	-.7187	-.2424	.079

Note. — No fits are given for the 1992 session, as these data are very unreliable. We do not recommend using these expressions for $\nu > 15$ GHz for dates prior to 1995, as the high frequency data for those dates have high errors.

3C123 is one of the non-variable objects that we have identified. The right panel of Fig. 7 shows the source’s secular flux density evolution, based on our polynomial expression for 3C286. Notable is a small ($\sim 1\%$) but significant drop at 1465 MHz, beginning in 2008. This drop is also seen at 1275 MHz in 2008, but at no other frequency utilized between 2008 and 2011. We believe the drop is real, but have no explanation for its origin.

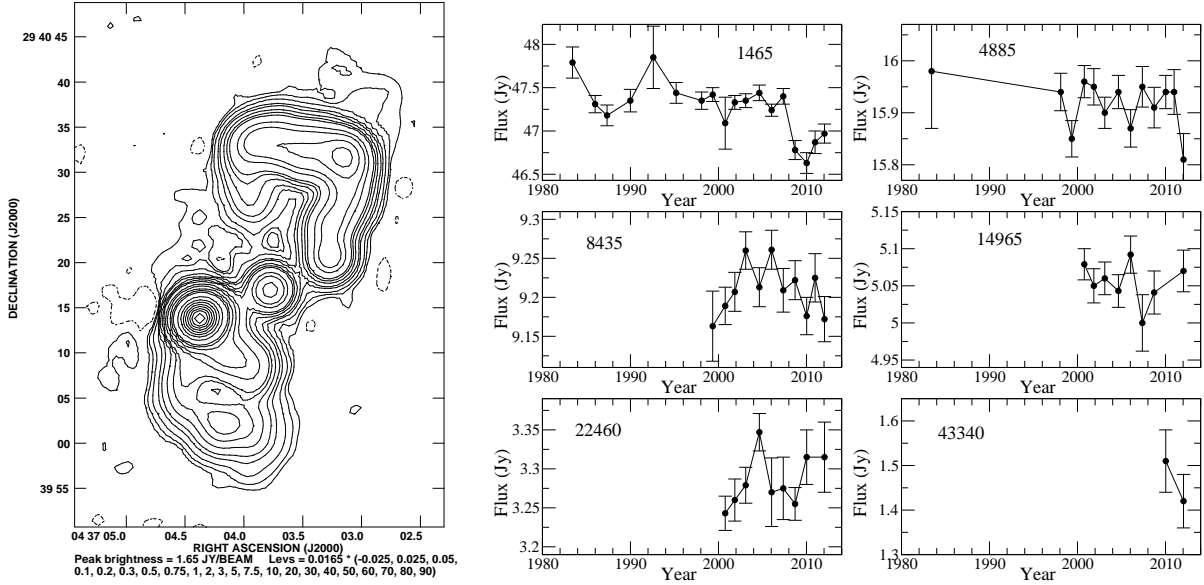


Fig. 7.— On the left panel, the structure of 3C123 at 22.485 GHz, with 3 arcseconds resolution. On the right panel, the secular variation of the observed flux density.

10.3. 3C138

3C138 is a compact step-spectrum quasar at redshift $z=0.759$. VLBI images show it has structure on a maximum scale of 0.62 arcseconds, with a highly polarized, one-sided jet leading from the nucleus, and some weak structure on the other side (Cotton *et al.* (1997a)). These structures are shown in a 60 milliarcsecond resolution VLA image at 43 GHz shown in Fig. 8. Due to its high flux density and small angular size, this source is commonly utilized by the VLA for amplitude gain calibration.

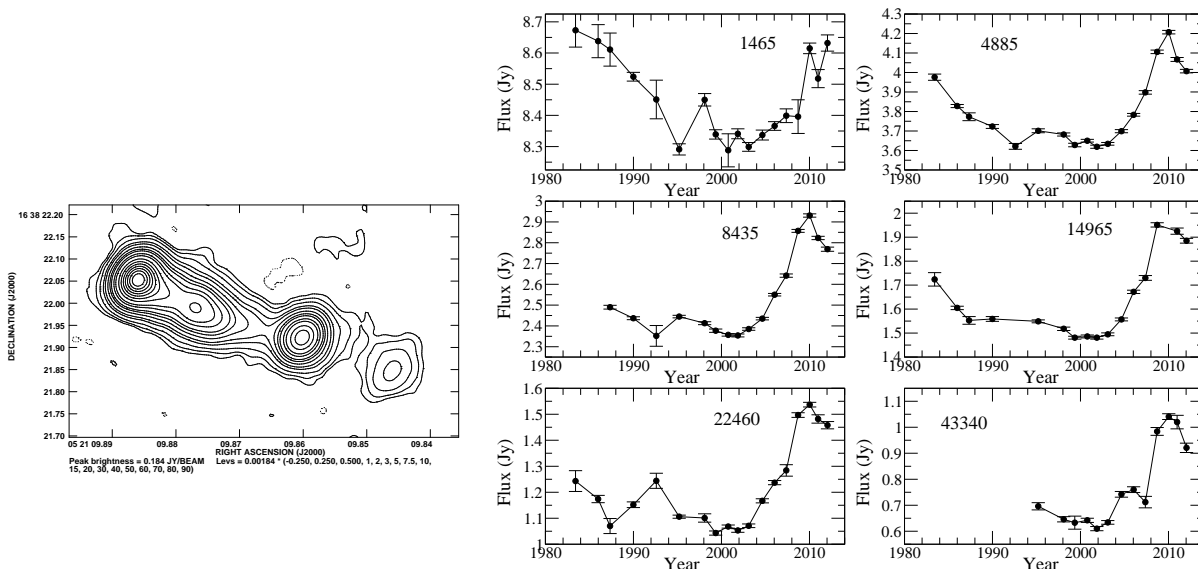


Fig. 8.— On the left panel, the structure of 3C138 at 43 GHz, with 60 milliarcseconds resolution. On the right panel, the secular variation of the observed flux density.

3C138 is not one of the Baars *et al.* (1977) sources, probably because it was known to be significantly variable. Our data show that this is indeed the case, with the slow decline noted after 1983 abruptly terminated with a large increase beginning in 2003, as shown in the right-hand side of Fig. 8. The flare, with the proportional increase being greatest at the higher frequencies (nearly doubling the flux density at 43 GHz), reached a peak in 2010, and is now quickly subsiding. We have fitted this variable spectrum with a cubic polynomial function for each of the 18 sessions, whose coefficients are given in Table 11.

10.4. 3C147

3C147 is a compact step-spectrum quasar at redshift $z = 0.545$. VLBI imaging shows structure of maximum extent of 200 milliarcseconds (Rossetti *et al.* (2009)). A VLA high resolution image at 43 GHz, made with high resolution data, is shown in the left panel of Fig. 9. The small angular size and high spectral flux density of 3C147 have resulted in

it being commonly used as a flux density scale calibrator by the VLA. This source has

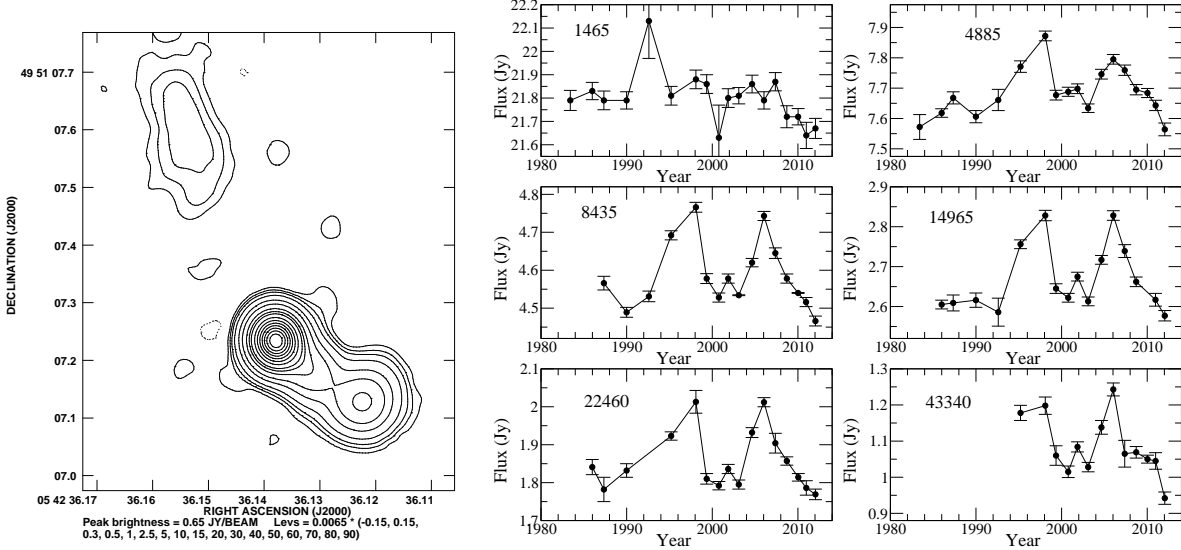


Fig. 9.— On the left panel, the structure of 3C147 at 43 GHz, with 60 milliarcseconds resolution. On the right panel, the secular variation of the observed flux density.

undergone significant changes in flux density over time, as shown in the right panel of Fig. 9. For all bands other than 20cm, a rise of 5 to 10% was seen between 1990 and 1998, again with the larger increases being seen at higher frequencies. This increase was followed by a sudden drop of similar magnitude lasting until 2004, then another short and rapid rise, of similar magnitude, to 2006. Since then, the flux density has been dropping steadily. We have fitted the variable flux densities of this source with cubic polynomials for each of the 18 observing session, the results of which are shown in Table 11.

10.5. 3C196

3C196 is a quasar at redshift $z = 0.871$. The source comprises a pair of compact lobes symmetrically placed about a weak core, with maximum angular extent of about 7 arcseconds, as shown in the 22 GHz, 1 arcsecond resolution image in the left panel of Fig. 10, made from the data taken for this program. In the right panel is shown the secular

variation. This source is one of the non-variable objects we have identified. Because of this,

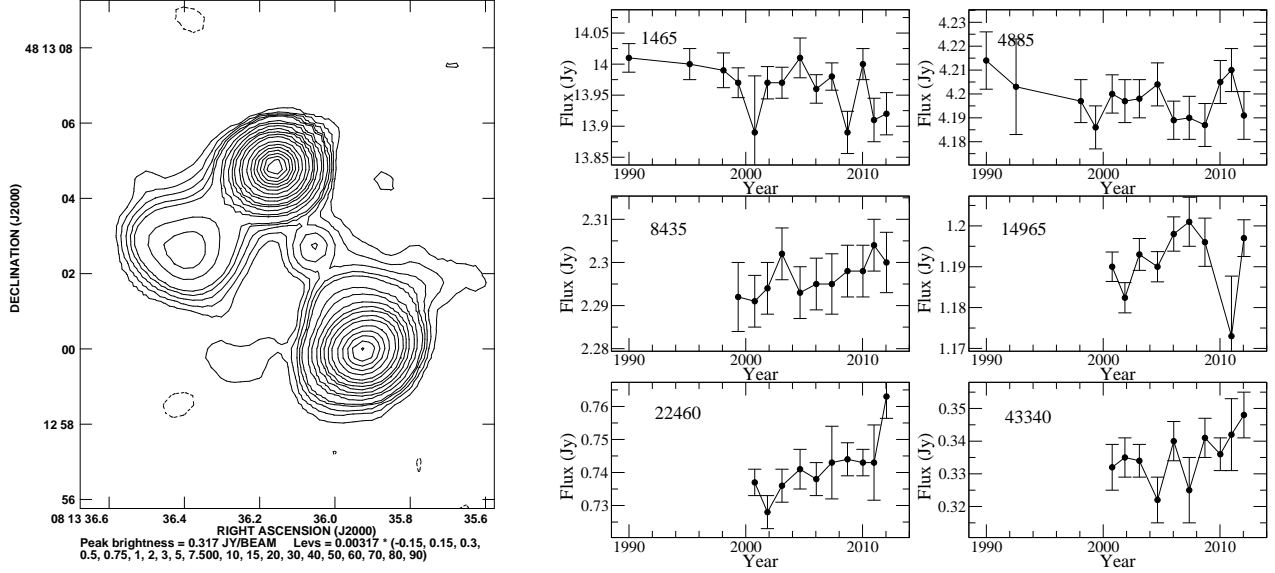


Fig. 10.— Left panel: The structure of 3C196 at 22 GHz, with 1 arcsecond resolution.

Right panel: The observed secular variation of this source.

its small angular size, and remarkably straight spectrum (Scaife and Heald (2012)), 3C196 is an excellent flux density calibration source for low-resolution observations for frequencies up to ~ 10 GHz.

10.6. 3C286

3C286 is a compact steep-spectrum quasar at redshift $z=0.846$. High resolution VLA images show the source has a steep-spectrum extension of length ~ 2.5 arcseconds to the SW, and a smaller knot of emission to the east, as shown in Fig. 11. VLBI, EVN, and MERLIN images show a highly polarized linear structure of maximum 50 milliarcseconds extent (Cotton *et al.* (1997b), Jiang *et al.* (1996), Akujor and Garrington (1995)). The milliarcsecond structure of this source has some very unusual features. The VLBA imaging shows that the compact central structure shown in the figure is steep spectrum, resolved to

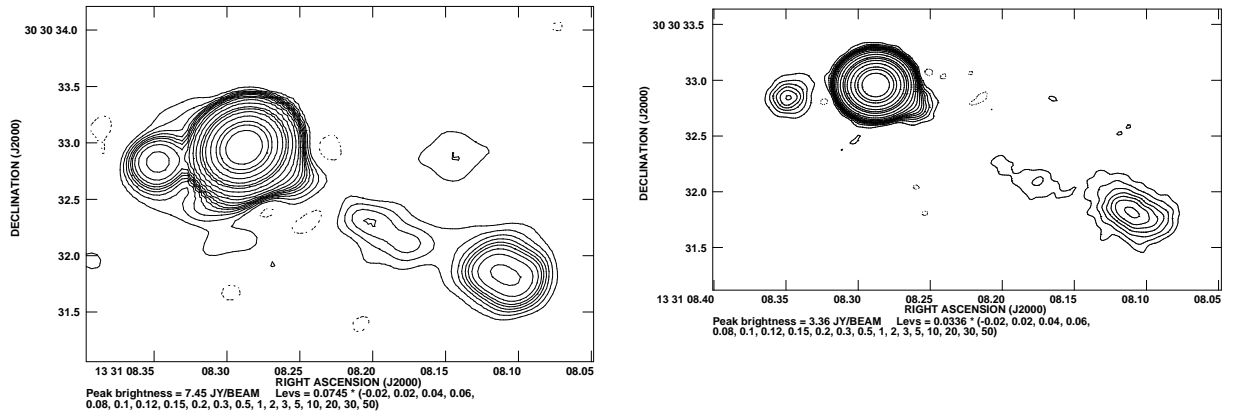


Fig. 11.— The structure in 3C286 at 5 GHz (left) with 310 milliarcsecond resolution, and at 15 GHz (right), with 220 milliarcsecond resolution.

the VLBA, and highly polarized throughout. There appears to be no optically thick central nuclear emission. It is doubtless the lack of the nucleus, and the uniform polarization visible in the maps of Cotton *et al.* (1997b) that make this object an extraordinarily stable and useful calibrator.

10.7. 3C295

3C295 is a radio galaxy at redshift $z = 0.464$. This source is a small double of ~ 5 arcseconds extent with very weak central nucleus, contributing less than 1% of the total flux density at 15 GHz (Taylor and Perley (1992)). An image of the source at 23 GHz with 1 arcsecond resolution, utilizing our data, is shown in the left panel of Fig. 12. In the right panel is shown the secular variation of the spectral flux density.

The weakness of the nuclear core emission suggests that this source should have a stable flux density, as noted by Ott *et al.* (1994). Our observations confirm this suggestion, showing no variation in its flux density to a level below 1% over the duration of our program. 3C295 is an excellent flux density calibration source for low-resolution interferometers below

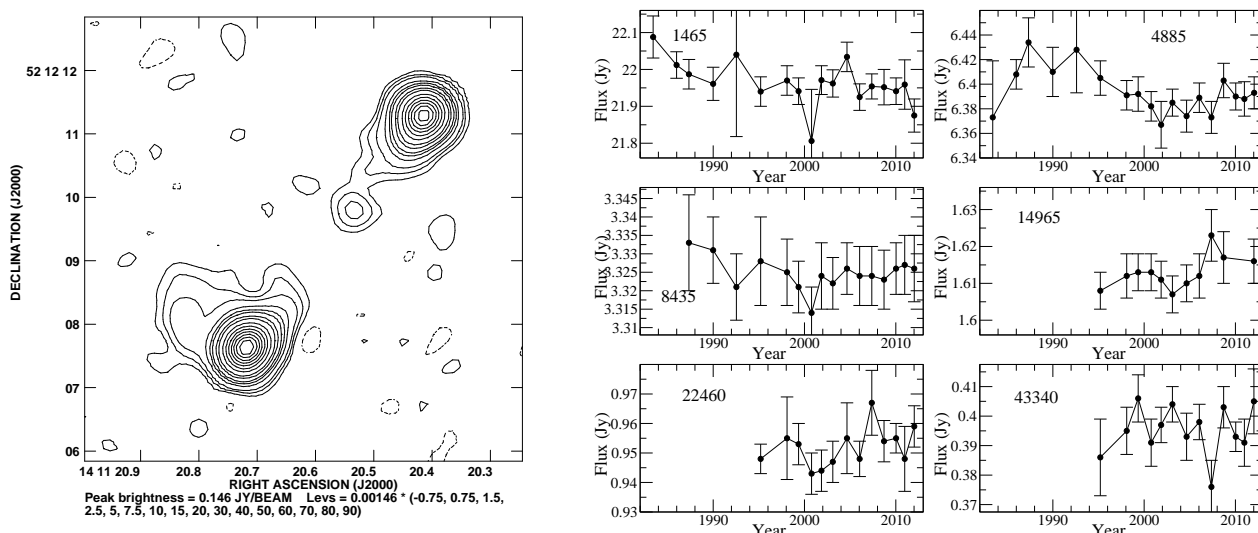


Fig. 12.— (left) The structure of 3C295 at 43 GHz with 1 arcsecond resolution. (right) The secular variation of the flux density in 3C295 – the source is clearly non-variable.

~ 10 GHz.

10.8. NGC6572

The planetary nebula NGC6572 was added to this program in 2000, based on its apparent similarity to NGC7027. The source is about 13 arcseconds in angular extent, with very diffuse emission extended to the north and south, as shown in Fig. 13. The lack of sharp edge emission makes the source a poor calibrator, as longer interferometer spacings provide insufficient amplitude to permit a stable gain solution for antennas located at the ends of the array. There is a possible trend in this source’s flux density over a 12-year timescale, as shown in the right-hand panel of the figure, showing the data, and a linear fit. The results of the fits are shown in Table 12.

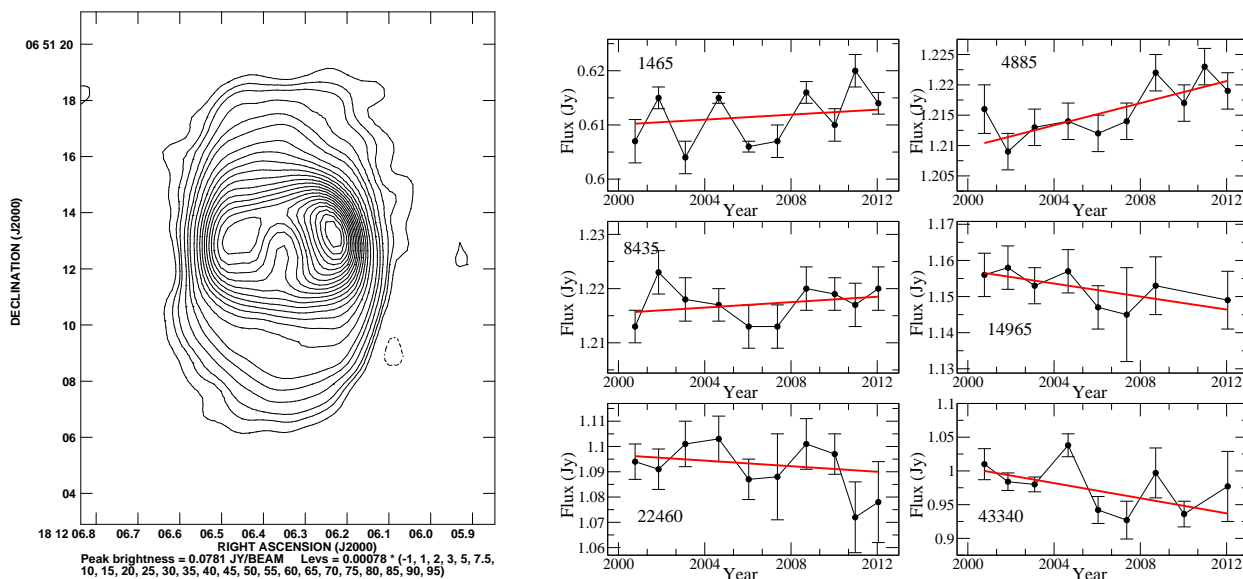


Fig. 13.— The structure of NGC6572: (left) At 22 GHz with 1.1 arcsecond resolution; (right) The secular variation in the flux density. There is marginal evidence for a secular evolution of the flux density. The results of a weighted linear fit to the data are superposed.

10.9. NGC7027

The bright, nearby planetary nebula NGC7027 is one of the Baars *et al.* (1977) sources. An image of the source at 43 GHz, made with our data and at 0.6 arcseconds resolution is shown in Fig. 14. Because of its large angular size, this source is not a good primary calibrator for high-resolution interferometers. NGC7027 has long been known to be increasing in flux density at the frequencies where it is optically thick, and to be decreasing at frequencies where it is optically thin. Zijlstra *et al.* (2008), using the data taken in this program up to 2006, utilized these secular variations, combined with optical observations of the linear expansion velocity and photo-ionization models, to place tight limits on the age and distance to the planetary nebula, and on the mass of the central star. The observations taken since 2006 show the flux density continuing to change as expected, but there is now some evidence of a deceleration in the secular increase at 1465 MHz, and also a possible deceleration in the secular decrease at 4885 MHz. The results of a weighted fit are given in

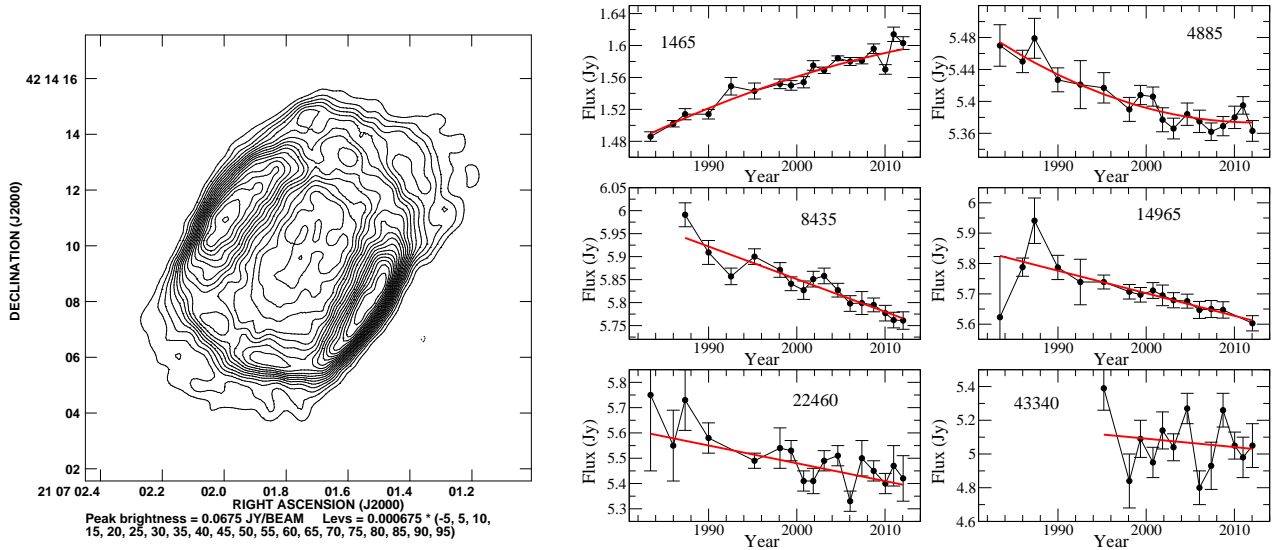


Fig. 14.— (left) The structure of NGC7027 at 43 GHz with 600 milliarcsecond resolution; (right) The secular variation of the source over the 30-year span of this program. The flux density is decreasing at all frequencies where the source is optically thin, and is increasing at 1465 MHz, where the source is optically thick. There is marginal evidence for a deceleration at the lowest two frequencies.

in Table 12, and plotted in the figure. We emphasize that the statistical significance for deceleration is low – further long-term monitoring will be needed to establish the reality of this result.

10.10. MWC349

MWC349 is a binary Be star of 2.4 arcseconds separation. We added this source to our monitoring list, following suggestions that it may be suitable as a flux density calibrator at long-millimeter and centimeter wavelengths. Its radio structure has been extensively studied by Tafaya *et al.* (2004) showing 0.3 arcsecond extent at 10 GHz, and 1 arcsecond at 3 GHz. A new, deeper image at 23 GHz with 1.1 arcseconds resolution with our data is shown in Fig. 15. The source is known to be variable in the visible, IR, and mm wavelengths

(Tafuya *et al.* (2004), and references therein).

Our observations show there are peculiar changes in the flux density of significant magnitude seen simultaneously over most bands. The most notable was in the Feb 2003 observations, when a drop in flux density of about 10% was seen at all frequencies except 1465 MHz. This drop cannot be due to pointing errors or atmospheric absorption, since these always affect high frequency observations much more strongly. A similar, but smaller, rise was noted in the Dec 2010 observations. It would appear that MWC349 has small but significant ($\sim 10\%$) changes in flux density. The changes are of short duration – less than one year. Because of these, the source is not a suitable absolute flux density calibrator for cm or mm wavelengths.

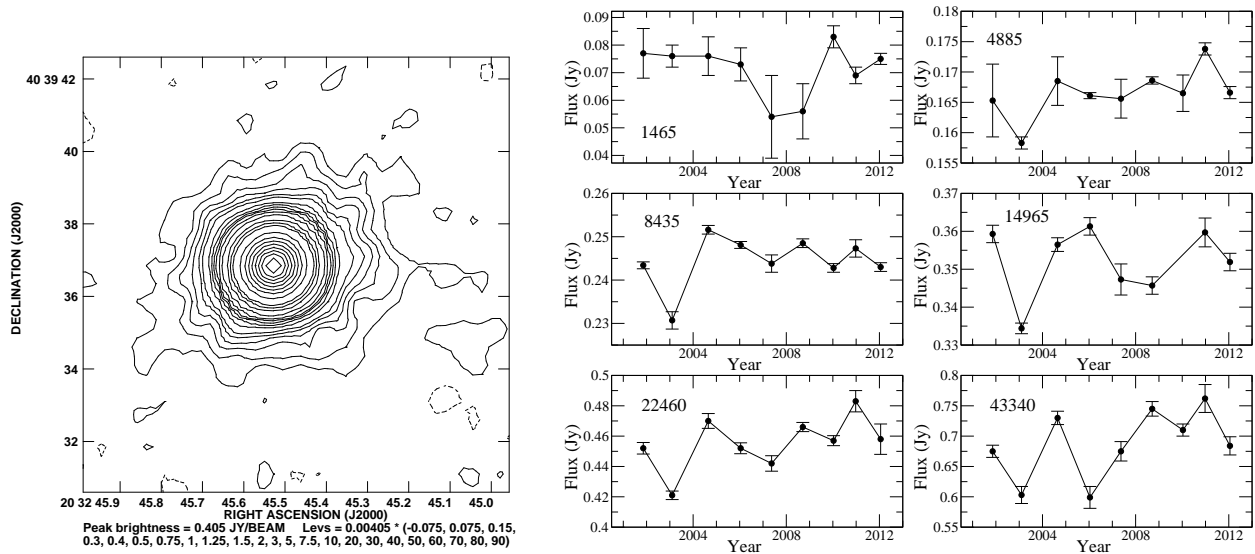


Fig. 15.— (Left) The structure of MWC349 at 22 GHz with 1.1 arcseconds resolution. A diffuse region of about 8 arcseconds extent surrounds the central core. (Right) Temporal Changes in the flux density for MWC349. The source shows significant short-term (one year, or less) variations in flux density.

11. The Planets

We added the planets Venus, Uranus, and Neptune (along with Mars) in 1995 in order to improve the model data for those objects. We show in Fig. 16 their emission in terms of their brightness temperature (properly accounting for the effect of the CMB background) at selected frequencies, taken from the observations in January, 2012. The secular variations –

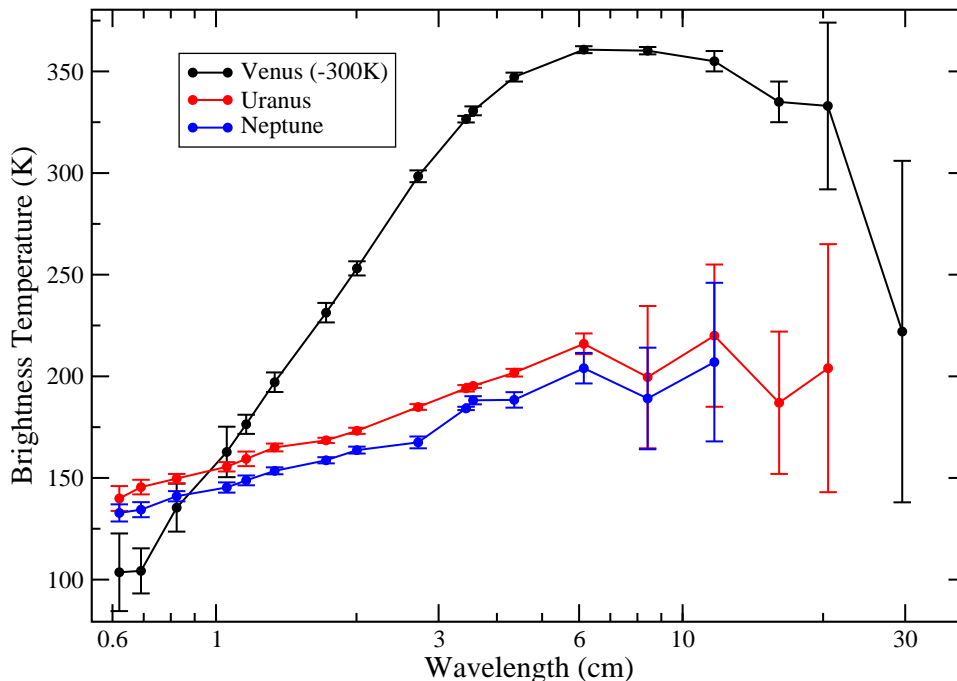


Fig. 16.— The brightness spectrum of the planets Venus, Uranus, and Neptune in 2012. Note that the brightness of Venus has been reduced by 300K.

if any – in the brightnesses at selected frequencies are shown in Fig. 17.

The emission from Venus is dominated at high frequencies by emissions from the atmosphere and at low frequencies by emissions from the surface; the crossover frequency is near 8 GHz, where the atmospheric opacity is approximately 1 (Muhleman *et al.* (1979)). The flux density of Venus at centimeter wavelengths has been described in Butler *et al.* (2001), and the curious low-frequency turnover discussed in Butler *et al.* (2004). Our observations match the higher-frequency model calculations but the decrease at low

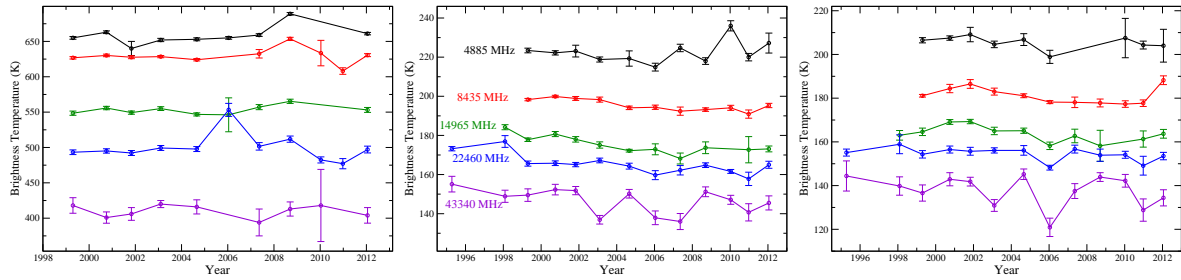


Fig. 17.— The secular variation in brightness for the three planets: Venus in the left panel, Uranus in the middle, Neptune on the right. The small variation for Uranus is due to its polar regions coming more into view.

frequencies is still unexplained. Venus is a suitable absolute calibrator for frequencies above 6 GHz, provided it is not too large for the telescope or interferometer, and provided it is not too near the Sun.

Radio emission from Uranus is entirely from the atmosphere, as the sensible surface is too deep in the planet. The flux density of Uranus at centimeter wavelengths has been described in Hofstadter and Butler (2003) and at millimeter wavelengths by Griffin and Orton (1993) (and references therein for both). Importantly, there is an enhancement of emission from both poles, and so viewing geometry changes the flux density significantly. Given the ~ 80 year orbital period of the planet, along with its unusual pole position relative to the ecliptic, variations on roughly decadal timescales are expected, and are clearly detected (Hofstadter and Butler (2003); Klein and Hofstadter (2006)). The expected flux density reached a minimum at the autumnal equinox in 2007, since the extent of the polar enhancements was minimized then, and we see this reflected in the measured flux densities. There is still some uncertainty as to whether these polar enhancements extend to millimeter wavelengths (Hofstadter *et al.* (2007)). Uranus is a suitable absolute calibrator at higher frequencies (above a few GHz, depending on the sensitivity of the telescope), up to the 50 GHz upper-limit of this study, as long as these geometry considerations are taken into account

Neptune is similar to Uranus in that its emission is entirely from the atmosphere. The differences are in the lack of geometry changes for Neptune (though there is also a south polar emission enhancement for Neptune, its sub-Earth latitude does not change appreciably over even decadal timescales), and differences in atmospheric composition (Deboer and Steffes (1996)). Neptune is a suitable absolute calibrator at the frequencies of this study as long as the sensitivity of the telescope is sufficient, though long-term studies of its emission are not as complete as for Uranus.

Detailed comparisons of our observed brightness temperatures with those predicted by various models are in preparation. We expect that these comparisons will result in improvements to the models of characteristics of the surfaces and atmospheres of these planets which will increase our understanding of them.

12. A Comparison with the Baars *et al.* (1977), and other Scales

One of the original purposes of this campaign was to determine the accuracy of the Baars *et al.* (1977) scale. The results are given in Table 13, where we give the ratio at six frequencies for the five sources 3C48, 3C123, 3C147, 3C286, and 3C295 between our Mars-based fluxes and the corresponding Baars *et al.* (1977) expressions. As three of the sources are shown here to be slightly variable, we have for these objects utilized the average flux densities over the measurement period. Note that although the Baars *et al.* (1977) scale for these sources is not defined above 15 GHz, we have applied their expressions to the higher frequency bands so users can conveniently estimate any flux density scale errors introduced by the use of these sources outside the recommended frequency range. Unsurprisingly, the deviations become quite large at these higher frequencies for most of these sources.

Table 12. Secular Evolution of NGC6572 and NGC7027

Freq MHz	NGC6572				NGC7027					
	S2000 mJy	Error mJy	Slope mJy/Yr	Error mJy/Yr	S2000 mJy	Error mJy	Slope mJy/Yr	Error mJy/Yr	Accel. mJy/yr ²	Error mJy/yr ²
1465	610	1	0.23	0.20	1561	2	3.6	0.2	-.05	0.02
4885	1210	2	0.91	0.27	5392	5	-3.0	0.4	0.12	0.05
8435	1216	2	0.25	0.30	5851	5	-7.1	0.7		
14965	1157	4	-0.9	0.7	5702	7	-7.4	1.1		
22460	1097	5	-0.6	0.8	5480	13	-7.0	2.0		
43340	1004	11	-5.6	2.1	5091	42	-5.0	6.3		

Table 13. Ratio of This Scale to the Baars Scale

Source	327.5 MHz	1465 MHz	4885 MHz	8435 MHz	14965 MHz	22460 MHz	43340 MHz
3C48	1.02	1.037	1.006	1.002	1.034	1.11	1.24
3C123	1.12	1.007	0.946	0.918	0.899	0.89	0.86
3C147	1.06	1.000	0.944	0.949	1.000	1.10	1.44
3C286	1.00	1.021	0.987	0.976	0.978	0.99	1.04
3C295	1.04	1.035	0.979	0.972	1.000	1.05	1.21

Note. — The ratios for the variable sources 3C48 and 3C147 are based on their long-term averages. Note that our proposed scale, at 327 MHz, is based on the spectral flux density of 3C196 given in Scaife and Heald (2012), and not on any absolute reference.

We also compared our new scale to the modified Baars scale proposed by Ott *et al.* (1994), and to the 34 GHz values for 3C48, 3C147, and 3C286, proposed by Mason *et al.* (1999), based on an absolute measurement made with the 1.5m OVRO radio telescope. The ratio of our values to those of Mason *et al.* (1999) are 0.97, 1.03, and 0.94, for the three sources. The mean ratio of 0.98 is within the cited errors of $\sim 6\%$ for Mason *et al.* (1999) and $\sim 2\%$ for our scale.

Ott *et al.* (1994) proposed modified versions of the Baars expressions for 3C286 and a number of other sources, using the Baars’ values for 3C295 as a reference. For our purpose, only their proposed expression for 3C286 is of interest. We show in Table 14 the values for selected frequencies. Note that Ott *et al.* (1994) utilized various observations of 3C295 at high frequencies to extend the Baars scale to 43 GHz. We conclude the high frequency extension of the Baars scale by Ott is low by up to 10% for frequencies above 15 GHz, with the error increasing with increasing frequency.

13. Summary

The VLA, when used with care, is capable of measuring the flux density ratios between compact, bright, and isolated radio sources with an accuracy much better than 1% at most frequency bands. We have utilized this capability to measure the ratios between a set of

Table 14. A comparison of ours, Baars, and Ott scales for 3C286

Scale	1465 MHz	4885 MHz	8435 MHz	14965 MHz	22460 MHz	43340 MHz
Baars	14.51	7.41	5.19	3.45	2.53	1.47
Ott	14.36	7.47	5.18	3.38	2.42	1.35
This paper	14.81	7.31	5.07	3.37	2.51	1.53

proposed calibration sources, covering the entire frequency range from 1 through 50 GHz. The observations span more than 30 years at some frequencies. The set of observed sources included seven compact extragalactic sources, two galactic planetary nebulae, one evolved star, and four planets.

The VLA cannot make accurate absolute measurements of the spectral flux density of radio sources. We converted our accurate ratio measurements to spectral flux densities by utilizing a thermophysical emission model of the planet Mars. The model was placed on an absolute scale by utilizing the WMAP observations of Mars, which are calibrated on the CMB dipole anisotropy.

From the nine compact, non-planetary objects, we determine that four sources – 3C123, 3C196, 3C286, and 3C295 are stable to within 1% over the 30-year span of this program at all frequencies except above ~ 40 GHz, where our accuracy is limited by antenna pointing. We present polynomial expressions for the spectral flux density of these four sources. Of these, 3C286 is the most compact with the flattest spectrum, on which basis we have selected it as our interferometric standard flux density calibrator. Using its derived spectrum, we determine the spectral flux densities of all the other sources over the frequency range of 1 to 50 GHz.

The three sources 3C48, 3C138, and 3C147 are commonly used flux density calibrators for the VLA and other interferometers. However, all are variable on timescales of several years. We have fitted polynomial expressions to their spectral flux densities as a function of time, to allow past users of the VLA to correct their calibration.

The planets Venus, Uranus, and Neptune are all potential calibration sources at high radio frequencies. Using our new scale, we have derived their mean brightness temperatures, to assist in improving models of their atmospheric emission.

The absolute accuracy of the new scale is estimated at $\sim 2\%$, with the largest source of error being the transfer of the WMAP observations to the VLA radio observations. The errors in the internal transfer from the derived spectral flux density of 3C286 to other sources is estimated at less than $\sim 1\%$ for all frequencies below ~ 20 GHz, and rises to $\sim 3\%$ at the highest VLA frequency of 50 GHz.

We emphasize that this very low error does not mean that all observations with the VLA have this accuracy. The actual accuracy obtained for any observation will, in addition to the estimated accuracy of the flux density scale, be determined by how the observation is set up, the observing conditions, and the care taken in the calibration and imaging steps.

The authors thank Eric Greisen for the many improvements made to the AIPS data reduction software package over the years of the project, particularly those needed in response to the dramatic increase in the VLA's capability with the implementation of the WIDAR correlator.

REFERENCES

- Akujor, C.E., and Garrington, S.T. 1995, *A&AS*, 112, 235
- An, T., Hong, X.Y., Hardcastle, M.J., Worrall, D.M., Venturi, T., Pearson, T.J., Shen, Z.-Q., Zhao, W., and Feng, W.X. 2009, arXiv:0910.3782v1
- Baars, J.W.M., Genzel, R., Pauliny-Toth, I.K.K., and Witzel, A. 1977, *A&A*, 61, 99
- Butler, Bryan 1996 ‘Tipping Considerations at the VLA’, VLA Scientific Memo 170
- Butler, Bryan 2002 ‘Atmospheric Opacity at the VLA’, VLA Test Memo 232
- Butler, B.M., and Bastian, T.S. 1999, in ‘Synthesis Imaging in Radio Astronomy II’, Taylor, G.B., Carilli, C.L., and Perley, R.A. (eds.) ASP Conference Series, 180, 625
- Butler, B.J., Steffes, P.G., Suleiman, S.H., Kolodner, M.A., and Jenkins, J.M. 2001, *Icarus*, 154, 226
- Butler, B.J., Campbell, D.B., de Pater, I., and Gary, D.E. 2004, *New A Rev.*, 48, 1511
- Conway, R.G., and Kronberg, P.P. 1969, *MNRAS*, 142, 11
- Cotton, W.D., Dallacasa, D., Fanti, C., Fanti, R., Foley, A.R., Schilizzi, R.T., and Spencer, R.E. 1997, *A&A*, 325, 493
- Cotton, W.D., Fanti, C., Fanti, R., Dallacasa, D., Foley, A.R., Schilizzi, R.T., and Spencer, R.E. 1997, *A&A*, 325, 479
- DeBoer, David R., and Steffes, Paul G. 1996, *Icarus*, 123, 324
- Greisen, Eric W. 2004, in ‘Information Handling in Astronomy – Historical Vistas’, A. Heck (ed.) *Astrophysics and Space Science Library*, 285, 109.
- Griffin, M.J., and Orton, G.S., 1993, *Icarus*, 105, 537

- Hofstadter, Mark D., and Butler, Bryan J. 2003, *Icarus*, 165, 168
- Hofstadter, Mark D., Butler, B.J., and Gurwell, M.A. 2007, *BAAS*, 39, 424
- Jarosik, N. *et al.* 2011, *ApJS*, 192, 14
- Jiang, D.R., Dallacasa, D., Schilizzi, R.T., Ludke, E., Sanghera, H.S., and Cotton, W.D. 1996, *A&A*, 312, 380
- Kestevan, M. ‘VLA Pointing’, VLA Test Memo 183
- Klein, M.J., and Hofstadter, M.D., 2006, *Icarus*, 184, 170
- Mason, B.S., Leitch, E.M., Myers, S.T., Cartwright, J.K., and Readhead, A.C.S. 1999, *ApJ*, 118, 2908
- Muhleman, D.O., and Berge, G.L., 1991, *Icarus*, 92, 263
- Muhleman, D.O., Ortaon, G.S., and Berge, G.L., 1979, *ApJ*, 234, 733
- Ott, M., Witzel, A., Quirrenbach, A., Krichbaum, T.P., Standke, K.J., Schalinski, C.J., and Hummel, C.A. 1994, *A&A*, 284, 331
- Perley, R. 2010 ‘On Determining Visibilities from Correlation Products’, EVLA Memo 145
- Rossetti, A., Mantovani, F., Dallacasa, D., Junor, W., Salter, C.J., Saikia, D.J. 2009, *A&A*, 504, 741
- Rudy, D.J., Muhleman, D.O., Berge, G.L., Jakosky, B.M., and Christensen, P.R. 1987, *Icarus*, 71, 159
- Scaife, Anna M.M., and Heald, George H. 2012 *MNRAS*, L30, 423
- Sidher, S.D., Griffin, M.J., Davis, G.R., Swinyard, B.M., Burgdorf, M., Orton, G.S., Rudy, D.J., Encrenaz, Th., Lellouch, E., and De Graauw, Th., 2000 *Icarus*, 147, 35

Taylor, G.B., and Perley, R.A. 1992, *A&A*, 262, 417

Tafoya, D., Gomez, Y., and Rodriguez, L.F. 2004, *ApJ*, 610, 827

Zijlstra, A., van Hoof, P.A.M., and Perley, R.A. 2008, *ApJ*, 681, 1296

Weiland, J.L. 2010 *ApJS*, 192, 19

Weiland, J.L., Odegard, N., Hill, R.S., Wollack, E., Hinshaw, G., Greason, M.R., Jarosik, N., Page, L., Bennett, C.L., Dunkley, J., Gold, B., Halpern, M., Kogut, A., Komatsu, E., Larson, D., Limon, M., Meyer, S.S., Nolta, M.R., Smith, K.M., Spergel, D.N., Tucker, G.S., and Wright, E.L. 2011, *ApJS*, 192, 1

Wright, E.L. 1976, *ApJ*, 210, 250